Impact of boundary conditions on onset and symmetry of precession-driven dynamos

Victor Botez,[1,*] André Giesecke,[2] Caroline Nore,[1] Loïc Cappanera,[3] and Frank Stefani[2]
[1]*Université Paris–Saclay, CNRS, Laboratoire LISN, F-91405 Orsay, France*
[2]*Institute of Fluid Dynamics, Helmholtz-Zentrum Dresden-Rossendorf, Bautzner Landstrasse 400, 01328 Dresden, Germany*
[3]*Department of Mathematics, University of Houston, Houston, Texas 77004, USA*

(Received 27 April 2026; accepted 20 July 2026; published 14 August 2026)

We numerically examine a kinematic dynamo driven by precession in a cylindrical geometry, with particular emphasis on the narrow range of Poincaré numbers where dynamo action is most likely at low and moderate magnetic Reynolds numbers. Using time-averaged velocity fields obtained from hydrodynamic simulations, we analyze the symmetry, oscillation frequency, and onset of the leading magnetic eigenmodes. Two competing families of magnetic fields are identified: a centrosymmetric, higher-frequency quadrupolar mode and a centroantisymmetric, lower-frequency dipolar mode. We then quantify how the dynamo threshold depends on the electromagnetic boundary conditions, including pseudovacuum versus true vacuum treatment and the presence of conducting and/or magnetically permeable vessel walls. We show that simplified vanishing-tangential-field boundary conditions systematically underestimate the critical magnetic Reynolds number, whereas realistic outer layers can either promote or suppress dynamo action depending on their electrical conductivity and on the selected hydrodynamic mean state. These results clarify the role of wall properties and mode selection for the forthcoming DRESDYN precession dynamo experiment.

DOI: 10.1103/rx1h-5zxp

I. INTRODUCTION

One of the open questions in the field of geophysical and astrophysical magnetohydrodynamics (MHD) is related to the energy source of hydromagnetic dynamos in planets and stars. Although thermal and/or compositional buoyancy is widely considered to be the most likely candidate, harmonic forcings such as precession and tides have been discussed as additional drivers of the geodynamo, particularly before the solid core formed. The actual dynamo effect resulting from these forces, however, is still under scrutiny [1,2]. Similar questions arise with regard to precession as a potential driver of the ancient lunar dynamo [3] or that of the asteroid Vesta [4]. A particularly interesting problem concerns the potential influence of the Milankovitch cycles on the reversal statistics of the geodynamo [5].

In addition to research dedicated to genuine geophysical and astrophysical problems, various attempts have been made to study the fundamental hydromagnetic dynamo effect in the laboratory [6,7]. These efforts, pioneered by the liquid sodium experiments in Riga [8–10] and Karlsruhe [11–13], have produced a wealth of interesting results on the self-excitation of magnetic fields in the kinematic dynamo regime and their backreaction in the saturated regime. Regarding the latter, the observation of magnetic field reversals in the von Kármán sodium (VKS) experiment [14–16]

[*]Contact author: botez@lisn.fr

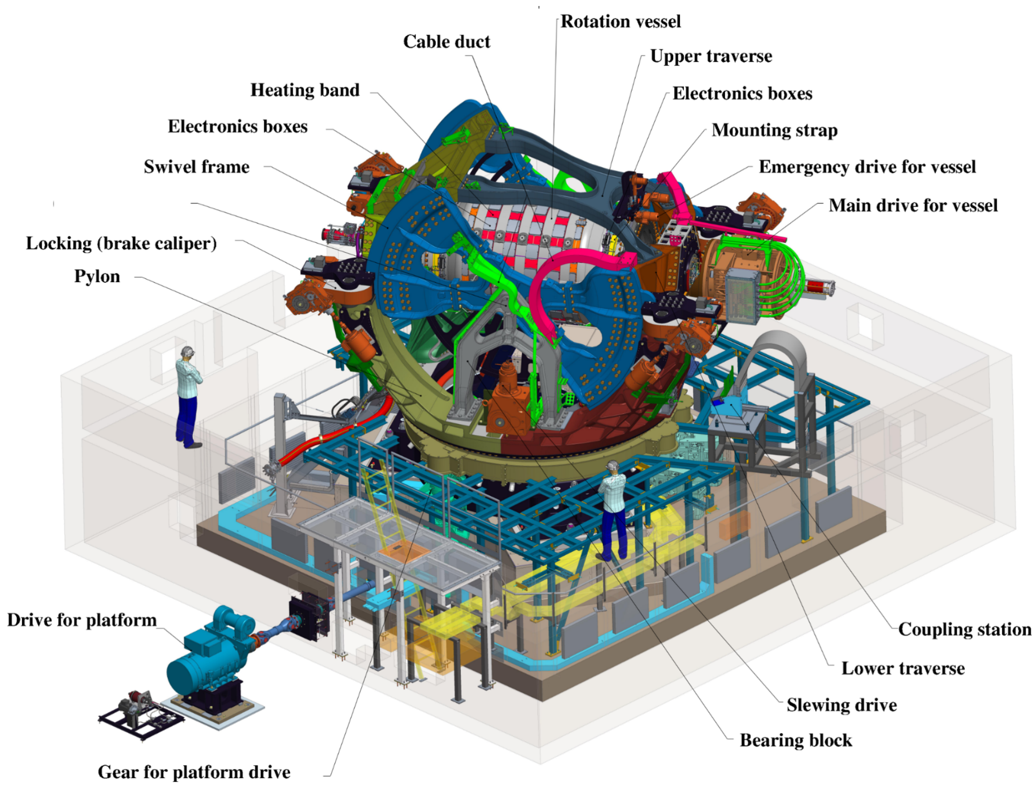

FIG. 1. View of the DRESDYN precession experiment with the main components indicated.

was an important milestone that has sparked renewed interest in paradigmatic mathematical models to explain the corresponding geomagnetic phenomenon [17–19]. This is just one example of how liquid metal experiments, while never providing perfect models of specific cosmic bodies, can indeed stimulate geophysical research.

In light of the growing importance of harmonic forcings in geophysical and astrophysical MHD, the next logical step appears to be the experimental realization of a precession-driven dynamo. Such an experiment (see Fig. 1), whose construction began a decade ago as part of the DRESden facility for DYNamo and thermohydraulic studies (DRESDYN) at Helmholtz-Zentrum Dresden-Rossendorf (HZDR) [20,21], is currently under commission [22]. Its central component is a stainless-steel cylinder measuring 2 m in both diameter (D) and height (H), which will be filled with liquid sodium. This cylindrical vessel is designed to rotate at 10 Hz around its axis and precess at up to 1 Hz around a different axis. As the body of liquid sodium is driven by rotation around two axes only, this machine would constitute the first homogeneous experimental dynamo, unaffected by internal walls, guiding tubes, or the use of ferromagnetic impellers.

Apart from the tremendous mechanical and technical challenges involved in constructing and operating such a machine, there is also a more fundamental physical issue to consider. Indeed, the flow structure and dynamo action of precession-driven flows are less predictable than in the Riga and Karlsruhe experiments. This problem is clearly related to the intended use of a homogeneous fluid, which flows much more freely than in those previous experiments.

The investigation of precession-driven flow has a long history, dating back to the early work of Sloudsky [23] and Poincaré [24], who had found an analytical solution for the flow of an inviscid fluid in a spheroidal cavity. This so-called Poincaré solution was later extended by Busse [25] to the weakly nonlinear regime, accounting for the effects of viscosity in boundary layers. In recent decades, precession-driven flows have also been studied in other geometries, and experiments have been carried out to understand various instabilities [26–28], large-scale vortex formation [29], and the transition to turbulence and its hysteretic behavior [30–35].

In preparation for the DRESDYN-precession experiment, significant numerical and experimental effort was dedicated to achieving a detailed understanding of the flow structure in a cylinder with aspect ratio $H/R = 2$ [31,36–40]. For a Reynolds number of 10 000, which is currently the upper limit for 3D direct numerical simulations (DNS), but also a practical lower limit for experiments, a consistent picture of the flow's dependence on the precession ratio and nutation angle has emerged [39]. Exemplified for the nutation angle of 90°, this picture shows as the most striking effect a transition from a large-scale, quasilaminar flow to a highly turbulent flow [40]. This transition, which occurs at a critical precession ratio of approximately 0.1, consists of a two-stage collapse of the directly driven flow, accompanied by a significant modification of the zonal flow and the emergence of an axisymmetric double-roll mode within a narrow range of the precession ratio.

The key role of this double-roll mode for the experimental realizability of a precession-driven dynamo was revealed in [36]. While dynamo action had been numerically found for precession in various geometries [36,41–48], the double-roll mode turned out to lower significantly the critical magnetic Reynolds number Rm. In the picture of [49], this can be understood in terms of the "dynamo-proneness" of the so-called s_2-t_1 flow, which comprises a poloidal double-cell flow (s_2) and a single-cell toroidal rotation (t_1). In the optimal case, the critical Rm was shown to be as low as 430 [36,37,39], which is indeed encouraging, given the technically achievable value of 700.

Strictly speaking, however, these low values were obtained only when simplified boundary conditions of the magnetic field were used. While a correct treatment would require a potential field to "fill" the vacuum surrounding the dynamo, so-called *vanishing tangential components* (VTC) conditions (which are often used to simplify the numerics) are known to underestimate the critical Rm. For the setting of the DRESDYN-precession dynamo, this was shown recently in [50].

The present paper aims to clarify this issue by simulating the DRESDYN-precession dynamo using the SFEMaNS code, which can correctly treat vacuum boundary conditions in cylindrical geometry. After describing the numerical setup, we will begin with the purely hydrodynamic problem and compare the results with previous findings. Then, based on the obtained flow fields, we will solve the kinematic dynamo problem for a variety of electrical and magnetic material parameters of the wall. Particular focus will be on two different symmetries of the emerging magnetic field and how they depend on specific boundary conditions. The paper will conclude with a summary and an outlook on the planned experiments.

II. SETUP

A. Numerical setup

We model the DRESDYN-precession flow with a cylinder of radius R and height $H = 2R$ such that its aspect ratio is $\Gamma = H/R = 2$. This aspect ratio is known to be close to the first resonance of the directly forced mode (see, e.g., [39,51,52]). The vessel rotates around its vertical axis at angular velocity $\Omega_c \mathbf{e_z}$ and precesses around an axis $\mathbf{k}$ which can make an angle α with the vertical axis such that the precession angular velocity reads $\Omega_p \mathbf{k}$. The general setup is sketched in Fig. 2. In the following, we will limit our study to the case of angle $\alpha = 90^\circ$ such that, up to a rotation in Cartesian coordinates, we can write the precession angular velocity as $\Omega_p \mathbf{e}_x$.

The nondimensionalization is the same as in [45]. The reference length is taken to be R, the radius of the cylinder, and the reference velocity is defined as $U_0 = R\Omega_c$. The fluid within the cylinder is considered incompressible such that we can define the reference pressure $P_0 = \rho U^2$, with ρ being the fluid's density. Then the electrical conductivity and magnetic permeability of the fluid are assumed constant and equal to σ_0 and μ_0, respectively, with μ_0 the magnetic permeability of the vacuum. The typical magnetic field scale is chosen so that the reference Alfvén speed is 1, namely $B_0 = U_0\sqrt{\mu_0 \rho}$. We then define three dimensionless parameters of the problem. The

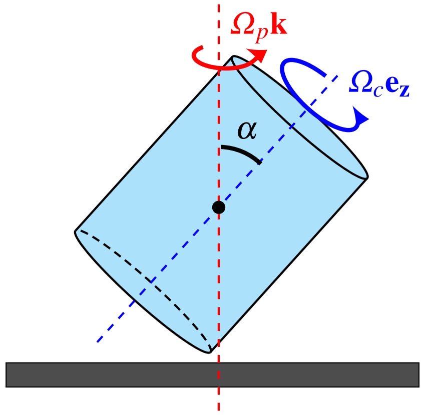

FIG. 2. Sketch of the precessing cylinder rotating around $\mathbf{e}_z$ and precessing around $\mathbf{k}$, the two axes forming an arbitrary angle α.

Reynolds number $\mathrm{Re} = R^2\Omega_c/\nu$, ν being the fluid's kinematic viscosity, measures the ratio between the velocity's advection and diffusion. Note that Re is in fact the inverse of the Ekman number Ek. The magnetic Reynolds number $\mathrm{Rm} = R^2\Omega_c\mu_0\sigma_0$ is the analogous parameter for the magnetic field considering Ohmic dissipation. Finally, the ratio between the precessing and rotating angular velocities is the Poincaré number and reads $\mathrm{Po} = \Omega_p/\Omega_c$ in the case $\alpha = 90^\circ$. Throughout this paper, we will only consider equations and quantities measured in the turntable frame of reference, i.e., the frame attached to the turntable in which the cylinder rotates with angular velocity $\Omega_c\mathbf{e}_z$. Considering the nondimensionalizations introduced so far, and the simplifications due to choosing $\alpha = 90^\circ$, we can write the Navier-Stokes equations in the turntable frame as follows:

$$\frac{\partial \mathbf{u}}{\partial t} + (\mathbf{u}\cdot\nabla)\mathbf{u} = -\nabla p + \frac{1}{\mathrm{Re}}\nabla^2\mathbf{u} - 2\mathrm{Po}\mathbf{e_x}\times\mathbf{u} + \mathbf{J}\times\mathbf{B}, \quad \nabla\cdot\mathbf{u} = 0, \tag{1}$$

with $\mathbf{u}$ and p being, respectively, the velocity and pressure fields. Likewise, the induction equations within the conductive domain read

$$\frac{\partial \mathbf{B}}{\partial t} = \nabla\times(\mathbf{u}\times\mathbf{B}) - \frac{1}{\mathrm{Rm}}\nabla\times\left[\frac{1}{\sigma_r}\nabla\times\left(\frac{\mathbf{B}}{\mu_r}\right)\right], \quad \nabla\cdot\mathbf{B} = 0, \tag{2}$$

while a much simpler equation applies to the scalar magnetic potential in the vacuum:

$$\Delta\phi = 0. \tag{3}$$

Throughout this paper, $\mathbf{B}$, $\mathbf{H} = \mathbf{B}/\mu_r$ and $\mathbf{J} = \nabla\times\mathbf{H}$ are, respectively, the magnetic induction field, the magnetic field, and the electric current density. $\mu_r = \frac{\mu(\mathbf{x})}{\mu_0}$ and $\sigma_r = \frac{\sigma(\mathbf{x})}{\sigma_0}$ are, respectively, the magnetic permeability and electrical conductivity relative to those of the fluid. They will be relevant when modeling solid walls separating the fluid-filled vessel and the vacuum. Finally, the magnetic field in the vacuum V^v, outside the conducting cylinder V^c, is modeled through a magnetic scalar potential ϕ such that $\mathbf{H} = \nabla\phi$. The set formed by Eqs. (1)–(3) constitutes the magnetohydrodynamic (MHD) equations.

In the Navier-Stokes equations, there are two forcing terms: the Coriolis force and the Lorentz force. The velocity field is subject to no-slip boundary conditions on the cylinder's walls, $\mathbf{u}_{|\partial V} = \mathbf{e}_\theta$ at $r = 1$ (sidewall) and $\mathbf{u}_{|\partial V} = r\mathbf{e}_\theta$ at $z = \pm 1$ (lid walls).

As for the magnetic field $\mathbf{H}$, several boundary conditions will be considered: either vanishing tangential components (VTC) $\mathbf{H}_{|\partial V^c}\times\mathbf{n} = \mathbf{0}$ (also called pseudovacuum conditions), or vacuum boundary conditions. In this second case, we solve for the magnetic scalar potential ϕ within a sphere of radius $r_{\text{sphere}} = 10$, at the edge of which we enforce Dirichlet boundary conditions $\phi(r_{\text{sphere}}) = 0$. Translating this onto $\mathbf{H} = \nabla\phi$, we get $\mathbf{H}_{|\partial V^v} \times \mathbf{n} = \mathbf{0}$ at $r_{\text{sphere}} = 10$.

B. SFEMaNS and the kinematic dynamo problem

We first simulate the Navier-Stokes equations with given flow parameters and simultaneously time-average the velocity field. The turntable framework is the only one in which the Navier-Stokes equations [Eqs. (1)] do not involve explicit time dependence, allowing us to safely consider time averaging. Next, the induction equations are solved with this time-averaged frozen velocity field. Throughout this paper, we will disregard the magnetic field's feedback on the velocity field, so that the magnetic field equations become linear. Dynamo instability is reached when the Ohmic dissipation proportional to $1/\text{Rm}$ is sufficiently low to allow exponential growth of the magnetic field.

The Navier-Stokes and the induction equations are solved using the HPC code SFEMaNS (for Spectral/Finite Elements for Maxwell and Navier-Stokes). This code uses hybrid spatial discretizations with spectral decomposition along the azimuthal direction and Lagrange polynomial elements in the meridional planes, with order 2 elements for the velocity and magnetic fields as well as the magnetic scalar potential (written P_2, third-order accurate), and order 1 for the pressure field (written P_1, second-order accurate). At Reynolds number $\text{Re} = 6500$, which we will consider in the following, we use a large eddy simulation (LES) stabilization method to solve for the velocity field. For details on this method, see [53–55]. The local mesh size for the computation of the pressure field is $h_{\text{loc}}^{\text{wall}} = 1/80$ close to the walls, $h_{\text{loc}}^{\text{top}} = 1/60$ at $r = 0$ and $z = \pm 1$, and $h_{\text{loc}}^{\text{origin}} = 1/40$ at the origin, and it is half the size for the velocity field. The azimuthal direction is resolved using 80 complex azimuthal Fourier modes. Time-stepping is performed using a second-order accurate BDF2 (backward differentiation formula) scheme with a time step $dt = 0.001$. Computations are parallelized on all Fourier modes and on two meridional sections (160 CPUs), such that $\Delta t = 200$ code times, amounting to approximately 32 cylinder's rotations, are computed in roughly 7000 CPU hours on 2×64 AMD nodes.

As for the induction part, several meshes were considered due to the numerous setups studied in the following. We always use 60 complex azimuthal Fourier modes. The vacuum outer shell, when accounted for, has local mesh size $h_{\text{loc}} = 1$ at its borders. The conducting domains are simulated with the magnetic induction field $\mathbf{B}$. In Sec. III B, the fluid and the conducting domains are identical and solved with the mesh described before, whereas Secs. III C and III D consider the addition of a thin wall of thickness $w = 0.03$ between the fluid-filled vessel and the insulating medium. In these setups, the magnetic induction field is solved on another mesh with P_2 local mesh sizes $h_{\text{loc}}^{\text{wall}} = 1/400$ at $r = 1$, $h_{\text{loc}}^{\text{bulk}} = 1/200$ at $r = 0.9$, $h_{\text{loc}}^{\text{top}} = 1/160$ at $r = 0$ and $z = \pm 1$, and finally $h_{\text{loc}}^{\text{origin}} = 1/80$ at the origin. These refinements are designed to handle the discontinuities induced in the outer wall, bearing in mind that the magnetic energy will be mostly confined close to the cylinder's walls. The time-stepping is performed with $dt = 0.002$. Computations are parallelized on all Fourier modes and at most four meridional sections (240 CPUs in total) such that $\Delta t = 200$ time-codes can be computed in around 7000 CPU hours. The divergence of $\mathbf{B}$ is controlled in a negative Sobolev norm that guarantees convergence under minimum regularity [56–58]. The continuity condition across conductor/insulator interfaces as well as the magnetic induction components' jump conditions are ensured by using an interior penalty method.

C. Centrosymmetry

The geometry that is considered here is symmetric with respect to centrosymmetry [59], which can be written as

$$\begin{aligned} r &\to r, \\ \theta &\to \theta + \pi, \\ z &\to -z. \end{aligned} \tag{4}$$

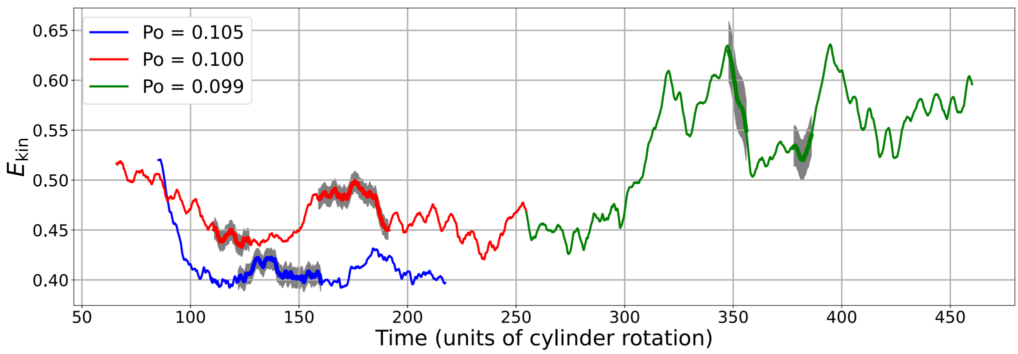

FIG. 3. Time evolution of the kinetic energy for different Poincaré numbers at Re = 6500 in the turntable frame. The areas shaded in gray and marked with thicker lines represent the intervals where time-averaging is carried out.

It is a combination of a rotation around the vertical axis and a reflection with respect to the $z = 0$ plane. Therefore, considering a vector field $\mathbf{f}$, its symmetric field with respect to centrosymmetry $\tilde{\mathbf{f}}$ is

$$\begin{aligned}\tilde{f}_r(r,\theta,z) &= +f_r(r,\theta+\pi,-z),\\ \tilde{f}_\theta(r,\theta,z) &= +f_\theta(r,\theta+\pi,-z),\\ \tilde{f}_z(r,\theta,z) &= -f_z(r,\theta+\pi,-z).\end{aligned} \tag{5}$$

Any vector field $\mathbf{f}$ can be uniquely written as a combination of its symmetric part $\mathbf{f}^s = (\mathbf{f} + \tilde{\mathbf{f}})/2$ and its antisymmetric part $\mathbf{f}^a = (\mathbf{f} - \tilde{\mathbf{f}})/2$ as $\mathbf{f} = \mathbf{f}^s + \mathbf{f}^a$. A centrosymmetric field is such that $\mathbf{f} = \tilde{\mathbf{f}} = \mathbf{f}^s$ while a centroantisymmetric field is such that $\mathbf{f} = -\tilde{\mathbf{f}} = \mathbf{f}^a$. $\mathbf{f}^s$ will also be called the symmetrized field or the restriction of the total (or raw) field $\mathbf{f}$ to $\mathbf{f}^s$.

III. RESULTS

A. Characterization of the velocity fields

In this section, we first describe the various types of velocity field that will be used in kinematic dynamo simulations later on. All simulations are carried out using direct numerical simulation (DNS) for all Reynolds numbers until reaching Re = 6500, after which we switch on a LES stabilization method. For details on this method, see [53–55]. At Re = 6500, according to [39], dynamo action is expected to occur at reasonably low values of Rm < 2000 for Po $\sim$ 0.100. In the following, we will consider the following three Poincaré numbers: Po = 0.099, 0.100, and 0.105. According to [39], the last two Poincaré numbers generate dynamo action for Rm $\sim$ 800 at a nutation angle $\alpha = 90^\circ$, while Po = 0.099 has not been explored yet.

The velocity field is simulated as follows: the Poincaré number is fixed at Po = 0.100 in the first place, while the Reynolds number is progressively increased from Re = 500, 1000, 2500, to Re = 6500. As in [45], the kinetic energy transitions from stationary to periodic, then quasiperiodic, and finally chaotic. For a more detailed analysis of the route to chaos, we refer to [31,37,40]. In Fig. 3 we show two runs with three hydrodynamical states Re = 6500 and Po $\in$ [0.099, 0.100, 0.105]. Both curves were started from Re = 6500, Po = 0.100 states.

Qualitatively, there is a clear difference between the average kinetic energies of the three simulations, with Po = 0.099 displaying spikes of strong kinetic energy and a higher average value. At Po = 0.100 and 0.099, we observe consistent deviations of the instantaneous kinetic energy, with variations of the order of 10% between the highest and lowest values, as opposed to the

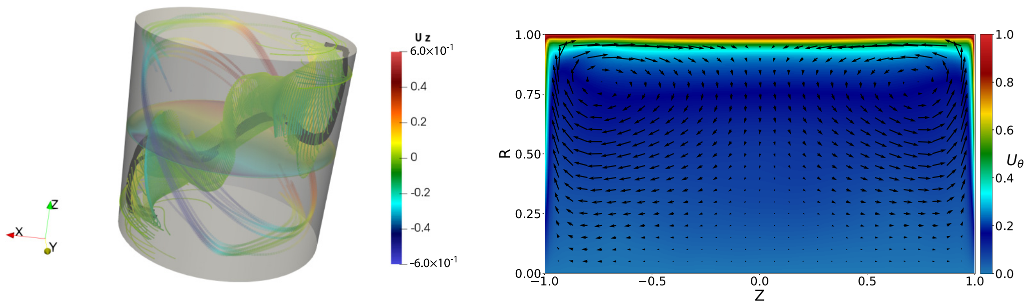

(a) (b)

FIG. 4. Representations of the mean velocity flow at Re = 6500 and Po = 0.100, for the high level of kinetic energy E_{kin}^{high}. (a) The black streamlines crossing the whole cylinder are vorticity lines, while the green lines surrounding the latter are velocity streamlines. The velocity streamlines and plane are colored by U_z, where red maps positive values and blue maps negative values. We remind the reader that the precession axis is $\mathbf{e}_x$. (b) Representation of the typical axisymmetric velocity. Arrows represent the two poloidal cells, while the colors show the toroidal component.

run at Po = 0.105. Qualitatively, these states can be defined over several cylinder rotations, as illustrated by the gray areas in Fig. 3. Kinematic dynamo simulations are usually performed using a velocity field that is averaged over a sufficiently long period in order to deduce a statistical magnetic eigenmode. For instance, in [37,50] time-averaging was performed over at least 100 rotation periods. In the present study, we examine the effect that midfrequency (i.e., slower than advection and faster than diffusion) oscillations around the mean energy of the large-scale flow have on the kinematic dynamo. Specifically, we consider velocity fields that are averaged over the shaded time windows shown in Fig. 3. At Po = 0.099, we examine the two time-windows $t \in [348, 356]$ and $t \in [378, 386]$. The corresponding flow energies will be labeled as E_{kin}^{low}(Po = 0.099) and E_{kin}^{high}(Po = 0.099). Likewise, at Po = 0.100 we consider two different time-windows: $t \in [111, 127]$ in the first "valley" of the kinetic energy, labeled E_{kin}^{low}(Po = 0.100), and $t \in [159, 191]$, which corresponds to the plateau at a higher level of kinetic energy, and labeled E_{kin}^{high}(Po = 0.100). As for Po = 0.105, which is the optimal Poincaré number for dynamo action according to [39], a single larger time window $t \in [122, 160]$ will be considered. We mention that the sampling frequency, 250 snapshots per rotation period, is high enough to capture the average large-scale flow and cancel out the faster uncorrelated small-scale oscillations for all time-windows. A typical shape of the 3D velocity field at the hydrodynamic parameters of interest is sketched in Fig. 4.

The vorticity lines in Fig. 4(a) allow us to identify the so-called spin-over mode, which characterizes precession-driven flows. At the relatively large Poincaré numbers considered here, this mode roughly goes through the entire cylinder from one corner to another in a plane close to the $y = 0$ plane (which is spanned both by the cylinder and the precession axes of rotation). There are mainly three large-scale structures, with their corresponding azimuthal Fourier mode m and vertical wave number k, that can be used to characterize this mean flow. The first two are as follows:

(1) The directly forced mode, or spin-over mode, which represents the direct response to the Poincaré forcing. It is composed of Kelvin modes with $m = 1$ and odd k. At aspect ratio $\Gamma = 2$, the dominating mode is $(m, k) = (1, 1)$.

(2) The axisymmetric toroidal component, which is composed of the axisymmetric U_θ component and is dominated by its geostrophic (or zonal) flow, with $(m, k) = (0, 0)$. In the following, it will be referred to as the zonal flow.

As detailed in [40,60], these two flow structures evolve jointly as the Poincaré number is increased until the transition to the turbulent regime is reached. Then, in a narrow window of Poincaré numbers [31], the directly forced mode, $(m, k) = (1, 1)$, weakens significantly. Its self-interaction

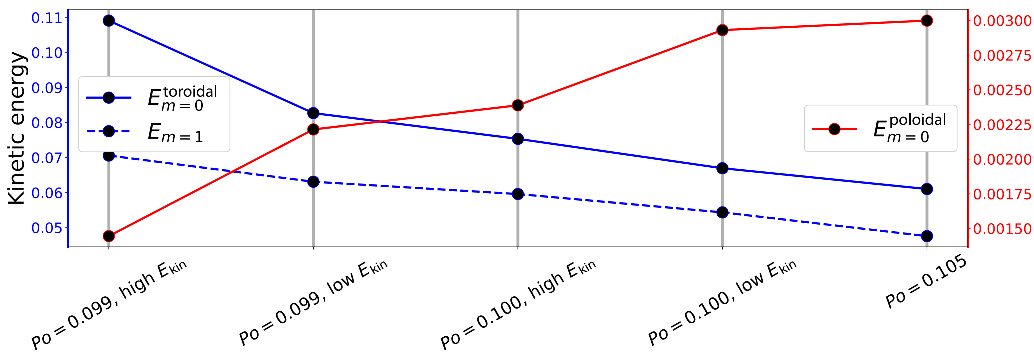

FIG. 5. Energy levels of the five velocity fields that emerge at different Po or for different time windows. The velocity fields are sorted with decreasing total kinetic energy (measured in the turntable frame).

through the advection term of the Navier-Stokes equation leads to the appearance of harmonics of $(m, k) = (1, 1)$, among which a third structure of importance appears:

(1) The double-roll mode, resulting from the self-interaction of the directly forced mode giving rise to a $(m, k) = (0, 2)$ mode (most energetic harmonic as seen in [40]). Its poloidal components U_r and U_z are of special interest to us.

In the following, the notions "toroidal" and "poloidal" will implicitly refer to the axisymmetric component of the velocity field. The double-roll mode, also called the nongeostrophic mode, can be observed by looking at an axisymmetric representation of the mean-flow as in Fig. 4(b). Obviously, it is composed of two poloidal cells in opposite circulation. Combining these two poloidal cells with the global zonal circulation (i.e., one toroidal cell) fits this kind of velocity field in the s_2-t_1 category of velocity fields according to [49], which is promising for dynamo action.

A quantitative comparison of the five different velocity fields extracted from Fig. 3 is performed in Figs. 5 and 6. The energies shown in Fig. 5 refer to the volume-integrated axisymmetric poloidal and toroidal components and to the $m = 1$ mode. We sort the five flow fields by total kinetic energy, which decreases due to energy loss in both the $m = 1$ and the toroidal mode. This is in contrast to the poloidal double-roll mode, which becomes stronger. Clearly, our selection of time windows covers well the first half of the Poincaré window, during which the transition to turbulence occurs and the double-roll mode appears [40]. From Po $= 0.099$ (high E_{kin}) to Po $= 0.105$, the poloidal component's kinetic energy gains a factor of 2, going from 0.75% to 2.5% of the total kinetic energy. Conversely, the zonal flow and the directly forced mode lose nearly 50% of their energy: while they represented $\sim$97% of the total energy for Po $= 0.099$ (high E_{kin}), they only account for $\sim$92% at Po $= 0.105$.

Focusing on the axisymmetric components, i.e., zonal flow and double-roll mode, a more quantitative picture of all five velocity fields is sketched in Fig. 6(a) (poloidal double-roll mode) and in Fig. 6(b) (toroidal zonal flow). For clarity, we choose to represent only the symmetrized poloidal field [Eq. (5)] in Fig. 6(a) considering, as shown in Sec. III B, that the antisymmetric component of the velocity field has little impact on the dynamo. Note that the toroidal $m = 0$ field is by definition symmetric with respect to the $z = 0$ plane.

The vertical components at radius $r = 0.9R$ [Fig. 6(a)] clearly mirror the two poloidal cells previously seen in Fig. 4(b). Moreover, at this particular radius, the axisymmetric component U_z shows increasing maxima and mean-amplitudes with decreasing total kinetic energy in accordance with Fig. 5: the highest value is achieved for Po $= 0.105$, while Po $= 0.099$ (high E_{kin}) shows amplitudes 2.5 times weaker. Moving on to the azimuthally averaged U_θ at $z = 0$ for $0 < r < 1$, with Fig. 6(b) representing the axisymmetric toroidal component, we notice a decrease of the mean values with decreasing mean energies (the maximum value remains equal to 1 due to no-slip boundary conditions at $r = 1$). In fact, the way we sorted the velocity fields by decreasing total

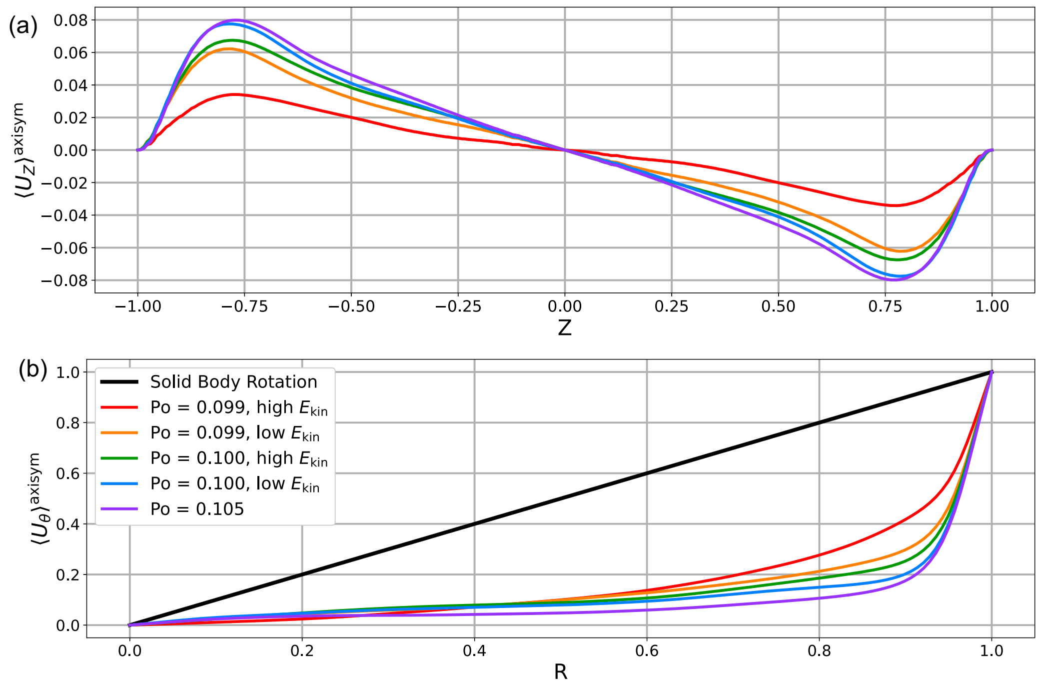

FIG. 6. Mean profiles of the axisymmetric time-averaged velocity field for different Poincaré numbers and time windows. (a) Representation of the poloidal double-roll mode: time and azimuthal average of U_z as a function of z at radius $r = 0.9$. Note that all profiles have had their antisymmetric components (with respect to centrosymmetry) removed. (b) Representation of the toroidal zonal flow: time and azimuthal average of U_θ as a function of r at height $z = 0$.

kinetic energies is correlated with the toroidal profile tending to zero outside of the boundary layer. This deviation from solid body rotation is typical of this geometry when keeping Re constant and increasing Po. The weakening of the U_θ component, which is opposite to what we described for U_z, is also compatible with Fig. 5. The zonal flow represents roughly 55% of the mean-flow kinetic energy, while the axisymmetric poloidal part is worth $\sim$1.5%, such that the joint decrease of the toroidal field (U_θ) and the increase of the poloidal field (U_z) results in a decrease of the global kinetic energy. To summarize, Figs. 5 and 6 show that the different levels of kinetic energy spotted in Fig. 3 can be explained by differences of the zonal flow and the directly forced mode.

As a side remark, bear in mind that the notion of "low" and "high" kinetic energy is solely used for practical reasons. If we had considered the cylinder's frame of reference, the labels would actually be inverted. In this case, the average kinetic energy would increase with Po rather than decrease. Again, this is related to the major part of the kinetic energy being contained within the axisymmetric toroidal component (see Fig. 5). Thus, when switching to the cylinder's reference frame, the kinetic energy of the toroidal component can be computed by measuring its distance to the solid body rotation in Fig. 6(b). As a result, the case Po $= 0.105$ would become the most energetic velocity field (deviating most from solid body rotation), and Po $= 0.099$ (high $E_{\rm kin}$) the weakest one (being closest to solid body rotation).

B. Kinematic dynamo in the no-wall configuration

In this section, we perform kinematic dynamo simulations using the five representative velocity fields studied in Sec. III A. At this point, we are considering the no-wall configuration, assuming the fluid-containing vessel is embedded in the vacuum and has infinitely thin walls. On these walls,

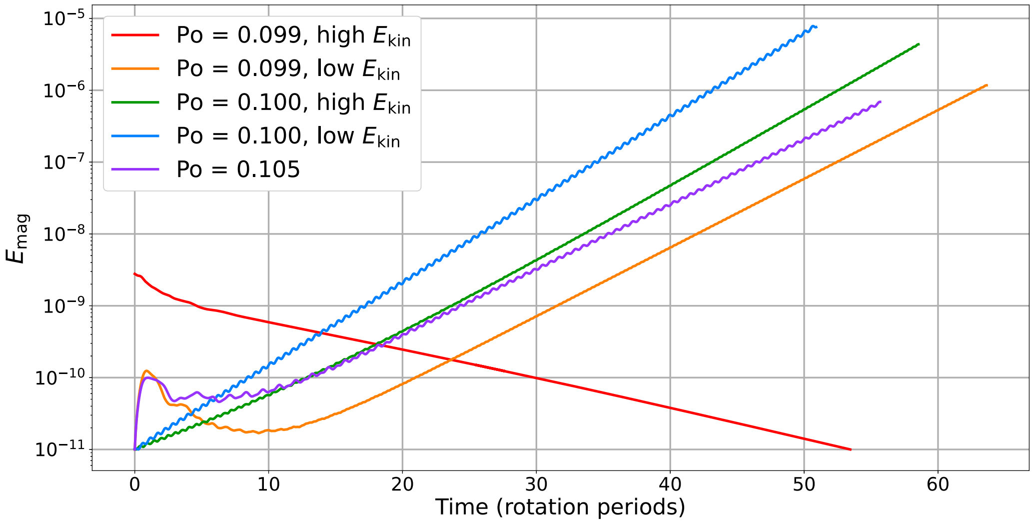

FIG. 7. Time evolution of the magnetic energy in the no-wall configuration, using vacuum boundary conditions, for five time-averaged but nonsymmetrized velocity fields. Rm = 1500 in all cases. Note that the velocity fields with the lowest kinetic energy (Po = 0.105 and 0.100, low $\mathrm{E_{kin}}$) generate oscillatory eigenfields with high amplitude and low frequency while the two velocity fields with intermediate kinetic energy (Po = 0.100, high $\mathrm{E_{kin}}$ and Po = 0.099, low $\mathrm{E_{kin}}$) generate oscillatory eigenfields with low amplitude and high frequency. The decreasing eigenmode (for Po = 0.099, high $\mathrm{E_{kin}}$) is nonoscillatory.

we will either consider vacuum boundary conditions, i.e., continuity of the magnetic field with the empty space, or pseudovacuum boundary conditions, i.e., $\mathbf{H} \times \mathbf{n} = \mathbf{0}$, in which case we do not solve for the magnetic field in the vacuum. Figure 7 shows the time evolution of the magnetic energy recorded for the five different velocity fields, using vacuum boundary conditions and always the same magnetic Reynolds number Rm = 1500.

Note that the magnetic energy computed using $\mathrm{E_{kin}^{high}}(\mathrm{Po} = 0.099)$ is the only one showing a negative growth rate and no oscillations. All other growth rates are complex-valued with a positive real part and a nonzero imaginary part. Seemingly, the oscillations of these dominating eigenmodes can be classified into two families: one with low frequency and high amplitude encompassing $E_{\mathrm{kin}}(\mathrm{Po} = 0.105)$ and $E_{\mathrm{kin}}^{\mathrm{low}}(\mathrm{Po} = 0.100)$, and the other one with high frequency and a low amplitude encompassing $E_{\mathrm{kin}}^{\mathrm{high}}(\mathrm{Po} = 0.100)$ and $E_{\mathrm{kin}}^{\mathrm{low}}(\mathrm{Po} = 0.099)$.

Representative 3D visualizations of the high-frequency eigenfield generated with $E_{\mathrm{kin}}^{\mathrm{high}}(\mathrm{Po} = 0.100)$ are shown in Figs. 8 and 9, and movies are provided in the Supplemental Material [61]. The magnetic fields are described by isosurfaces of their magnitude, colored by the vertical component of the magnetic field. The eight snapshots are equally spaced across one period of oscillation of $\mathbf{H}$, which corresponds to two periods of oscillations of $\mathrm{Em} = \int_{V^c} \frac{\mathbf{B}\cdot\mathbf{H}}{2} d\tau$. In each of these snapshots, there are six isosurfaces and they span the cylinder obliquely. When pairing each of these six cells with their centrosymmetric equivalent, we can describe these structures by three pairs of cells. The symmetric cells alternate the sign of their vertical component B_z, indicating that this magnetic eigenmode is primarily symmetric with respect to centrosymmetry. This is made more obvious by the representation from Fig. 9, which allows us to identify a quadrupole when observing the magnetic field lines in the vacuum from above. The succession of images also indicates that this (outer) quadrupole rotates along with the traveling inner magnetic field. In the following, we will often refer to this centrosymmetric, high-frequency eigenfield as the *quadrupolar mode*.

The inner magnetic field superimposed with the streamlines of the generating velocity field is represented in Fig. 10(a). At this intermediate Poincaré number Po = 0.100, the spin-over mode

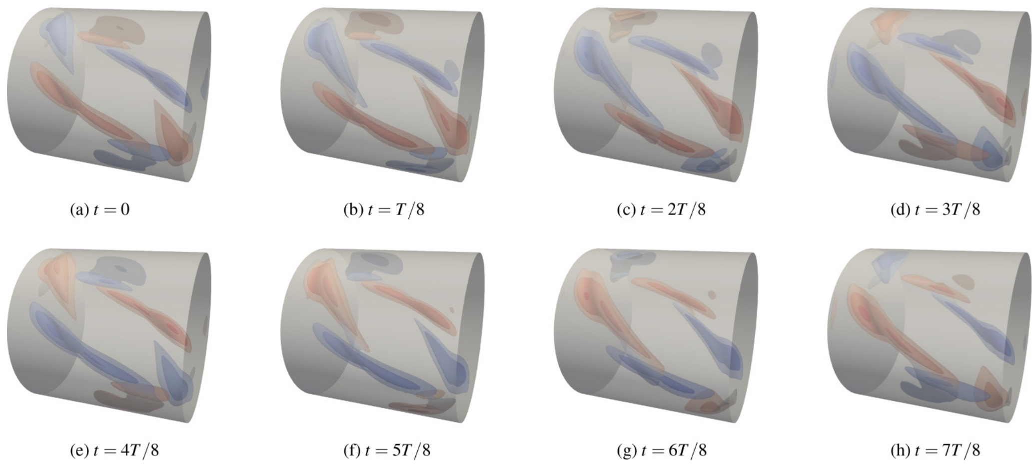

FIG. 8. 3D visualization (in the turntable frame of reference) of the centrosymmetric quadrupole mode inside the cylinder across a whole period. Its oscillation is of high frequency, period $T = 2\pi/\omega = 2.1$ (see Table I), and low amplitude. Isosurfaces are plotted at 25%, 50%, and 90% of the maximum magnetic field magnitude. Colors represent the vertical component, with red indicating positive values (towards the right) and blue indicating negative values (towards the left).

is S-shaped, and vorticity lines go through the entire cylinder in an oblique way with the velocity field lines rotating around them. Superimposing velocity lines and magnetic field isosurfaces shows how the magnetic cells travel periodically along the spin-over mode, encircling the vorticity lines. A finer analysis in azimuthal Fourier space is provided in Fig. 11(a), including the time evolution of the first few Fourier modes. Since the azimuthal modes $m = 0$ and 1 are the minimal ingredients to get dynamo action at low Rm [37], the growing magnetic field has to be a combination of several Fourier modes. In the present case, the most energetic Fourier modes are $m = 2$ and then $m = 3$, in

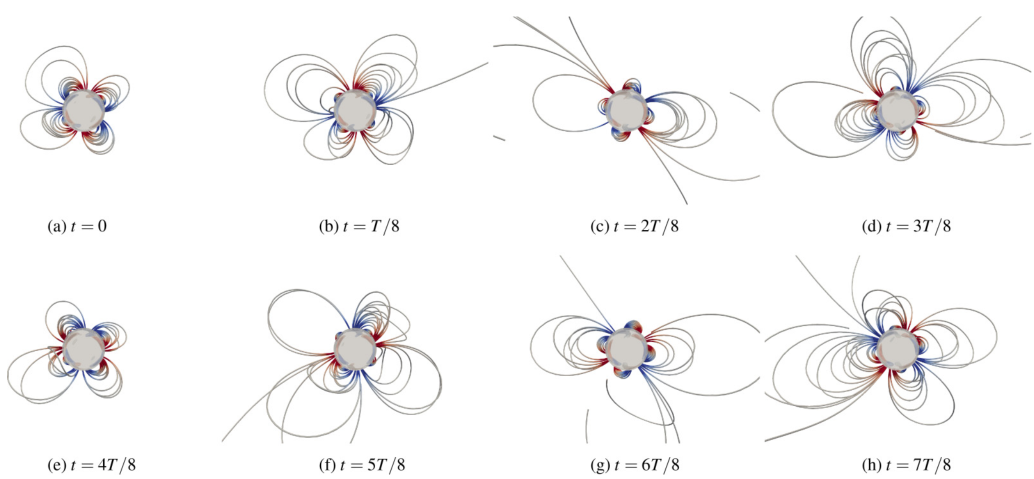

FIG. 9. Same as Fig. 8, but looking from above the cylinder. Inside the cylinder, isosurfaces are plotted at 25%, 50%, and 90% of the maximum magnetic field magnitude. Colors represent the vertical component, with red indicating positive values (towards the observer) and blue indicating negative values (opposite to the observer). Outside the cylinder, the streamlines of the magnetic field are colored by their r-component, red being positive and blue negative. They rotate counterclockwise.

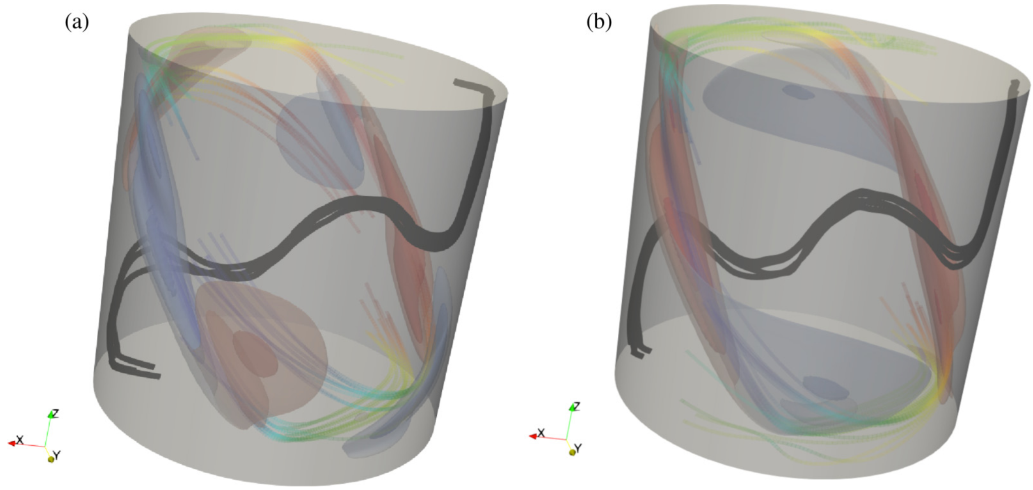

FIG. 10. 3D visualization of the joint magnetic-velocity-vorticity fields associated (a) with the symmetric (quadrupolar eigenmode) and (b) with the antisymmetric (dipolar) eigenmode. Magnetic isosurfaces are the same as in Figs. 8 and 12. Velocity streamlines are colored with their vertical component. The black lines crossing the cylinder, representing the spin-over mode, are vorticity lines.

accordance with the number of cells inside and the quadrupole outside. We mention that the Fourier spectrum in the vacuum is dominated by modes $m = 1$ and 2, while $m = 3$ becomes negligible, as should be any $m > 2$ for a general quadrupole.

A similar analysis can be carried out for the low-frequency eigenfield. This time, only four cells can be identified (Fig. 12), and we realize that this second eigenmode is mainly antisymmetric with respect to centrosymmetry. Once again, this becomes more obvious when examining the outer magnetic field lines, which are qualitatively those of a rotating oblique dipole (Fig. 13). The dominant azimuthal Fourier modes in Fig. 11(b) are $m = 1$ and 2 in accordance with the two pairs

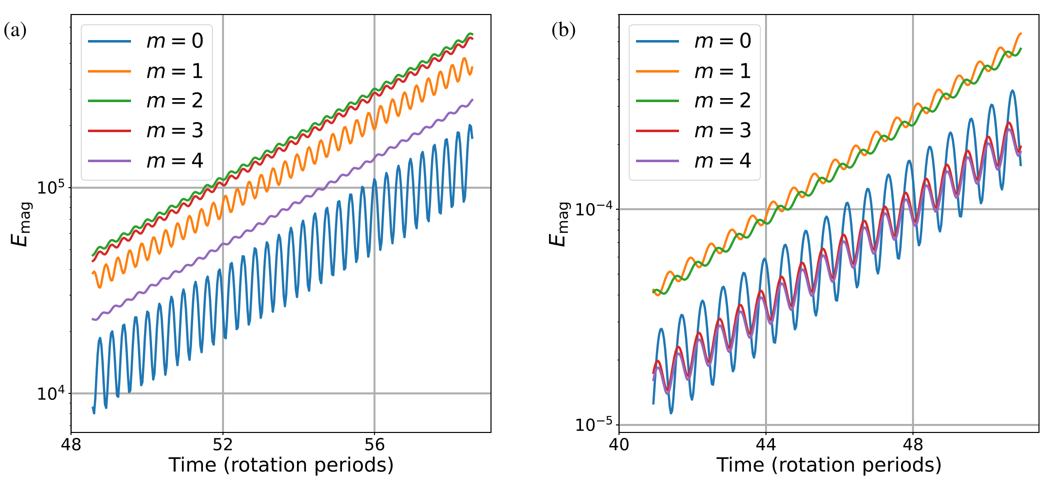

FIG. 11. Time evolution of the azimuthal Fourier modes of the magnetic energy in the no-wall configuration with vacuum boundary conditions for $\mathrm{Po} = 0.100$ at $\mathrm{Rm} = 1500$. (a) In the high kinetic energy time window, azimuthal Fourier modes $m = 2, 3$ are dominating. (b) In the low kinetic energy time window, azimuthal Fourier modes $m = 1, 2$ are dominating.

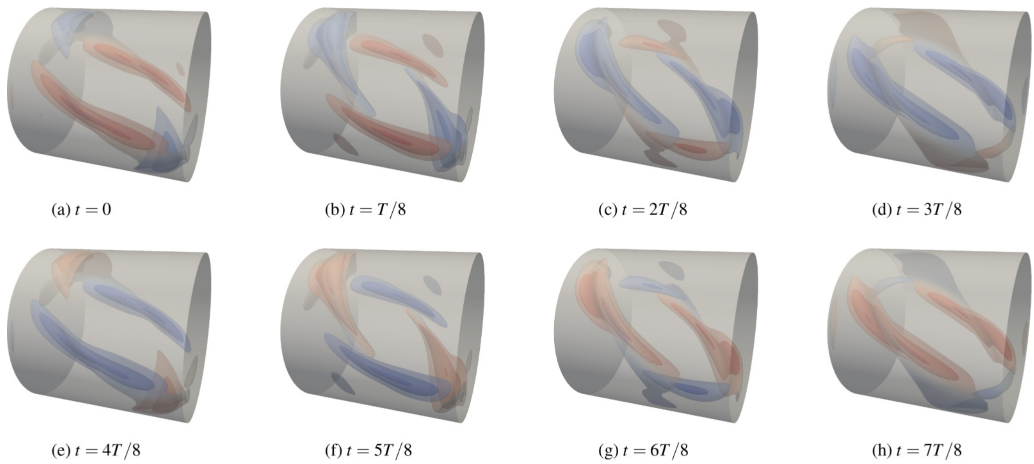

FIG. 12. 3D visualization (in the turntable frame of reference) of the centroantisymmetric dipole mode inside the cylinder across a whole period. Its oscillation is of low frequency, period $T = 2\pi/\omega = 3.7$ (see Table I), and high amplitude. Isosurfaces are plotted at 25%, 50%, and 90% of the maximum magnetic field magnitude. Colors represent the vertical component, with red indicating positive values (towards the right) and blue indicating negative values (towards the left).

of cells in the conducting domain. In the following, we will refer to this eigenfield as the *dipolar mode*. The Fourier spectrum of this mode in the vacuum is dominated by modes $m = 0$ and 1, while $m = 2$ becomes negligible, as should be any $m > 1$ for a dipole. Movies showing its oscillations are provided in the Supplemental Material [61].

The two magnetic modes that we just described are quite similar in structure, differing mainly in that they are either purely symmetric or purely antisymmetric with respect to centrosymmetry. The emergence of such eigenmodes is facilitated by the fact that the velocity field is almost purely centrosymmetric, the ratio of antisymmetric to total kinetic energy being close to 2% for all five

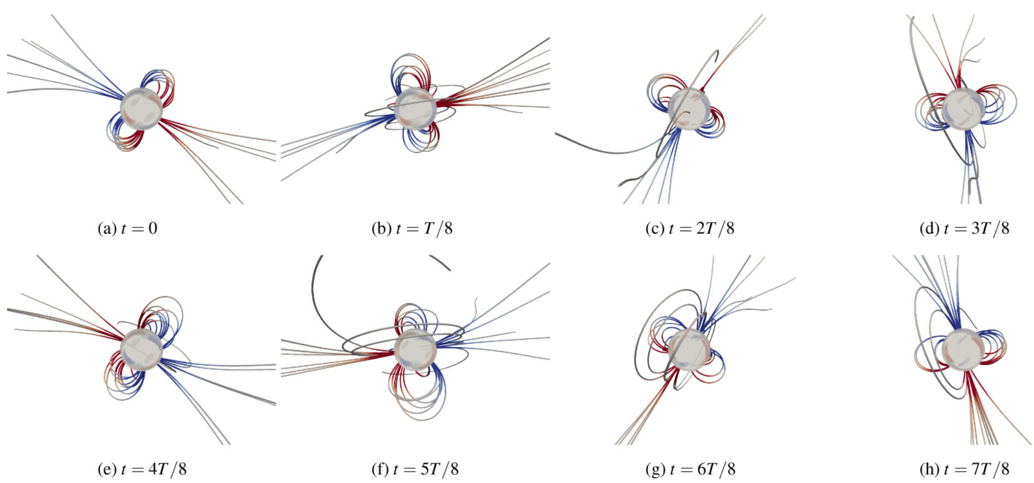

FIG. 13. Same as Fig. 12, but looking from above the cylinder. Inside the cylinder, isosurfaces are plotted at 25%, 50%, and 90% of the maximum magnetic field magnitude. Colors represent the vertical component, with red indicating positive values (towards the observer) and blue indicating negative values (opposite to the observer). Outside the cylinder, we observe streamlines of the magnetic field colored by their r-component, red being positive and blue negative. They rotate counterclockwise.

TABLE I. Characterization of the two dominant eigenmodes. The standard deviations are taken over all considered flows.

Feature eigenmode	Dipole	Quadrupole
Centrosymmetry	Antisymmetric	Symmetric
Fourier content	$m = 1, 2$	$m = 2, 3$
Inner cells	4	6
Oscillation frequency	$\omega = 1.72 \pm 0.12$	$\omega = 3.10 \pm 0.12$
Oscillation amplitude	$A = (4.97 \pm 0.61) \times 10^{-2}$	$A = (8.94 \pm 0.88) \times 10^{-3}$

time averages. The similarities in their inner magnetic field structures can be recognized in Fig. 10. For both eigenfields, at that specific stage of the oscillation, the cylinder's diagonals are occupied by a single pair of cells, the difference being within the endcaps, where the quadrupole fits two pairs of cells as opposed to the dipole, for which there is only one pair of cells that occupies a larger volume.

In the following, we will study the quadrupole and dipole modes jointly. Their main characteristics are summarized in Table I, where the amplitude A and angular frequency ω are determined by fitting the magnetic energy with the ansatz $f(t) \propto [1 + A\cos(\omega t)]e^{\lambda t}$.

Considering that in either case the cells rotate inside the cylinder counterclockwise with similar velocities, we can understand that the period of oscillation scales like $T \propto 1/N$, with N the number of pairs of cells, such that we get $\frac{\omega_{\text{anti}}}{\omega_{\text{sym}}} \propto \frac{2}{3}$, which is quite correct with regard to Table I.

Until now, our focus has been on the spatial structures of the two different oscillatory eigenfields at fixed magnetic Reynolds number $\text{Rm} = 1500$. We have identified two modes with similar structures but opposite symmetry, arising from two mean velocity fields that are very close in the hydrodynamic parameter space. Such pure eigenmodes occur as long as the mean-velocity field is perfectly centrosymmetric. It is therefore possible to track various eigenmodes of distinct symmetries by time integration if we solve the kinematic dynamo problem with the symmetrized velocity fields.

Figure 14 summarizes a few kinematic dynamo calculations for different velocity fields. Each simulation can be performed with the raw velocity field or with its symmetrized variant, equivalent to tracking the dipole and quadrupole simultaneously. Moreover, we can enforce two types of boundary conditions on the cylinder's wall, i.e., either the simplifying VTC (or pseudovacuum) conditions ($\mathbf{H} \times \mathbf{n} = \mathbf{0}$) or the correct vacuum conditions. Note that Fig. 14 shows only a part of the results, while all dynamo thresholds and magnetic field types are summarized in Table II.

Again, fitting the magnetic energy with the function $f(t) = (1 + A\cos\omega t)e^{\lambda t}$ provides the oscillation parameters in addition to the growth rates. The bold thresholds in the "sym" columns (for symmetric) have oscillatory parameters $\omega_{\text{quad}} = 3.10 \pm 0.12$ and $A_{\text{quad}} = 0.008\,94 \pm 0.000\,88$, with a small standard deviation across all data points. Conversely, the bold thresholds in the "anti" columns (for antisymmetric) have oscillatory parameters $\omega_{\text{dip}} = 1.72 \pm 0.12$ and $A_{\text{dip}} = 0.0497 \pm 0.0061$, again with a small standard deviation. We interpret those very minor variations of oscillation frequencies and amplitudes as the signatures of the quadrupolar field for the symmetric eigenmode and the dipolar field for the antisymmetric eigenmode. The complete fits of the growing magnetic energy, if they are oscillating, therefore allow us to identify which of the modes is growing. The other thresholds in Table II, which are not in bold, represent different eigenmodes, mostly nonoscillatory and decreasing for $\text{Rm} < 2000$, one exception being the magnetic field generated using $\text{Po} = 0.099$ (high E_{kin}) subject to VTC boundary conditions. For this case, the isosurfaces inside the fluid-filled container (drawn as in Figs. 8 and 12) shows four pairs of cells, which suggest that the eigenmode could be an octupole when looked at outside the vessel.

Note that there is a systematic $30 - 40\,\%$ difference between the thresholds obtained using VTC and vacuum boundary conditions, which is rather consistent with previous numerical findings for the VKS experiment [55,62]. In the case of symmetrized velocity fields, the two indicated thresholds

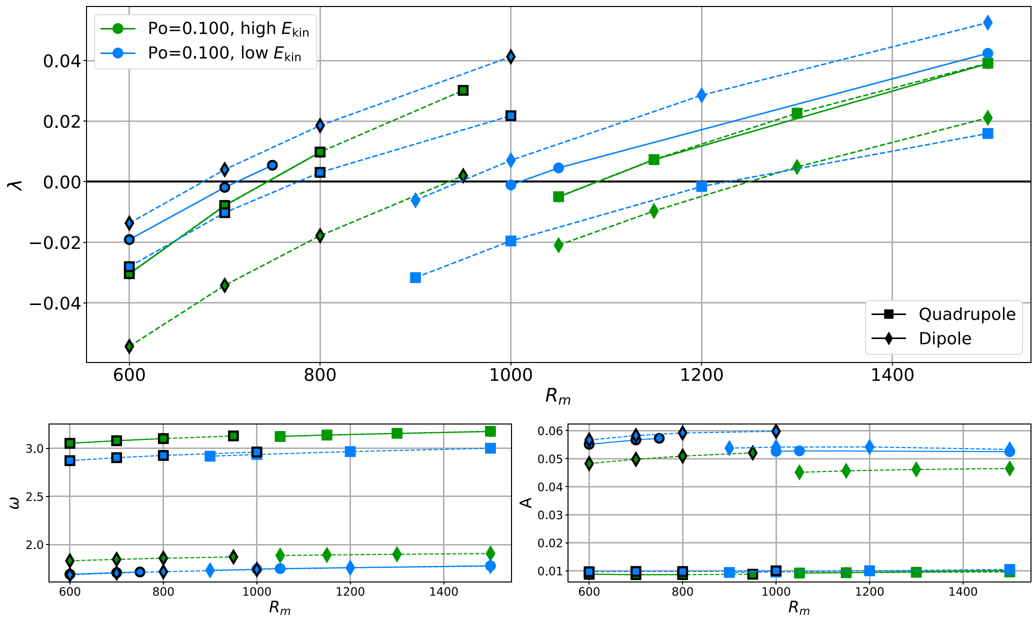

FIG. 14. Kinematic dynamo characteristics at $\mathrm{Po} = 0.100$ using the low and high kinetic energy velocity fields. The plots represent the growth rate λ and the oscillating parameters, namely the angular frequency ω and the amplitude A, of the magnetic energy as functions of Rm. The fits are performed using the function $f(t) \propto [1 + A\cos(\omega t)]e^{\lambda t}$. The curves' colors map the time-averaged velocity field used for the computations. Solid lines were computed using the full velocity field, while dashed lines only considered the symmetric component of the velocity field. The latter allows us to keep track of $\mathbf{B}_{\mathrm{sym}}$ (quadrupole, square markers) and $\mathbf{B}_{\mathrm{anti}}$ (dipole, diamond markers) simultaneously. Markers surrounded with black were computed using VTC boundary conditions, while the other ones were computed with a vacuum outer shell.

correspond to the symmetric and antisymmetric eigenvectors, respectively. It can be seen that, for a given fixed velocity field, the eigenmode that becomes unstable for the lowest Rm^c is always the same, regardless of whether the velocity field is symmetrized or not and regardless of whether VTC or vacuum boundary conditions are employed. Listing the magnetic eigenmodes by decreasing order of kinetic energy of the generating velocity field, the velocity field $\mathrm{Po} = 0.099$ (high E_{kin}) yields very high dynamo thresholds, above $\mathrm{Rm} = 1800$ even with VTC boundary conditions. Then the velocity field $\mathrm{Po} = 0.099$ (low E_{kin}) shows dynamo thresholds $\mathrm{Rm}^c < 2000$ for the quadrupolar and dipolar modes, although quite high for the dipolar mode, with $\mathrm{Rm}^c_{\mathrm{VTC}}(\mathrm{dipole}) = 1304 > \mathrm{Rm}^c_{\mathrm{vacuum}}(\mathrm{quadrupole})$. Considering afterwards $\mathrm{Po} = 0.100$ (high E_{kin}), the quadrupolar mode is still the critical mode, while this time the dipolar mode shows lower dynamo thresholds. Moving on to $\mathrm{Po} = 0.100$ (low E_{kin}), both modes still have similar thresholds, with the difference being that the dipolar mode now has a lower dynamo threshold than the quadrupole. Finally, the velocity field for $\mathrm{Po} = 0.105$ only generates an unstable dipole, while no unstable symmetric eigenmode can be spotted at $\mathrm{Rm} = 2000$.

This analysis shows that the quadrupolar and dipolar eigenmodes can coexist at $\mathrm{Po} = 0.100$, while this is unlikely for $\mathrm{Po} = 0.099$ and 0.105. In addition, the two magnetic fields' optimal thresholds regarding the specifics of the velocity field are different in the two cases. Indeed, the dipole's Rm^c decreases when switching from the high level to the low level of kinetic energy at $\mathrm{Po} = 0.100$, while it is the opposite for the Rm^c of the quadrupole. Thus, we can imagine that allowing the velocity field to vary with time would lead to a competition between these two modes. Our choice of considering small averaging time-windows does not allow us to properly define a dynamo threshold for given hydrodynamical parameters, namely $\mathrm{Re} = 6500$ and $\mathrm{Po} \in [0.099, 0.100, 0.105]$.

TABLE II. Dynamo thresholds in different configurations. The fluid-filled cylinder is either subject to VTC boundary conditions or directly in contact with the outer vacuum shell. Bold thresholds show oscillatory features of the quadrupole when in a symmetric column and of the dipole when in an antisymmetric column (see Table I). Thresholds above $\mathrm{Rm}^c = 2000$ were computed by extrapolating from the dominant eigenmodes at $\mathrm{Rm} = 1900$ and 2000, which are nonoscillatory.

Average velocity field	$\mathrm{Po} = 0.099, \mathrm{E}_{\mathrm{kin}}^{\mathrm{high}}$		$\mathrm{Po} = 0.099, \mathrm{E}_{\mathrm{kin}}^{\mathrm{low}}$		$\mathrm{Po} = 0.100, \mathrm{E}_{\mathrm{kin}}^{\mathrm{high}}$		$\mathrm{Po} = 0.100, \mathrm{E}_{\mathrm{kin}}^{\mathrm{low}}$		$\mathrm{Po} = 0.105$	
Boundary condition / eigenmode symmetry	sym	anti	sym	anti	sym	anti	sym	anti	sym	anti
vacuum raw	·	3568	**1149**	·	**1091**	·	·	**1009**	·	**1018**
vacuum symmetrized	3767	3944	**1154**	**1727**	**1090**	**1250**	**1227**	**946**	3954	**996**
VTC raw	·	1900	**804**	·	**735**	·	·	**713**	·	**685**
VTC symmetrized	4399	1897	**798**	**1304**	**745**	**935**	**777**	**677**	3728	**665**

Therefore, our results cannot really tell which of Po = 0.100 and 0.105 would provide a lower dynamo threshold. Taking this into account, the results are not incompatible with those from [63], which state that the mean state at Po = 0.105 should give better chances of getting a dynamo at Re = 6500 than that at Po = 0.100.

Another conclusion to be drawn from Table II relates to the impact of the antisymmetric component of the velocity field on the dominant magnetic eigenmode. Symmetrizing the velocity field roughly yields a decrease of the dynamo threshold of about 3–5 % in the case of the dipole, while a negligible impact is seen for the quadrupole. This result aligns with [44], where no impact of velocity field symmetrization was observed, but contrasts with [41] where the asymmetry of the flow (although in a precessing sphere) was shown to play a positive role in the dynamo process.

To conclude this subsection, we compare our new set of results with those from Sec. IV B of [44]. That section considered the same setup at the different hydrodynamic parameters Re = 1200 and Po = 0.15. Since, according to [40], the critical Poincaré number for the appearance of the double-roll mode scales like $\mathrm{Po}^c[\mathrm{Re}] \propto \mathrm{Re}^{-1/5}$, the extrapolation from our parameters (Re, Po) = (6500, 0.100) to (Re, Po) = (1200, Po^c[Re = 1200]) = (1200, 0.153) suggests that the considered hydrodynamic regimes are comparable, and the one from [44] should exhibit a double-roll mode as well. Reference [44] showed a horizontal quadrupole in a saturated regime, which is not inconsistent with our conclusions. Moreover, the description of its Fourier content matches ours, and the oscillation frequency from the linear regime $\omega \sim 3.2$, which can be read from Fig. 7(a) in [44], agrees with that of Table I. As for the curves of the magnetic energy in [63] and [50], the oscillation frequencies measured from reading Figs. 5.1 and 6(a), respectively, are $\omega \sim 1.5$, in relatively correct agreement with Table I, and $\omega \sim 1.25$, showing a relatively high 50% difference. Note that, compared to [50], our oscillation frequency for a given eigenmode shows a small standard deviation, as we have considered an advection timescale rather than a diffusive one.

The 3D structures shown in [37,50] are antisymmetric, such as our dipole. However, they seem to differ in their shape, thus indicating that the magnetic modes might depend on the Reynolds number despite being in the Poincaré window for the double-roll mode.

C. Impact of electrical conductivity of the vessel

In this section, we examine the impact of a thin sidewall on the dynamo, and compare the results with those obtained in [37,45], and [50]. From now on, the configurations considered in the previous subsection will be referred to as *reference configurations*. As in the real DRESDYN facility, the thickness of the sidewall is set to $0.03\,R$. We fix its relative magnetic permeability μ_r^S to 1 while varying its relative electrical conductivity σ_r^S between 0.125 (approximately that of the real stainless steel wall) and 4.5 (approximately that of a hypothetical copper wall). Moreover, we restrict ourselves to vacuum boundary conditions at both the outer face of the sidewalls and the lids, where no wall is considered.

As for the generating velocity fields, we chose Po = 0.100 and considered again a "high level" and a "low level" mean flow, which in the reference configuration generated a dipole-dominated and a quadrupole-dominated eigenfield, respectively. Their dynamo thresholds, obtained with either vacuum or VTC boundary conditions, can be found in Table III. The slight difference of the values for the $E_{\mathrm{kin}}^{\mathrm{high}}$ case compared to those of Table II is due to the use of a different velocity field. In particular, this modified $E_{\mathrm{kin}}^{\mathrm{high}}$ flow can exhibit a growing oscillatory dipole, although exclusively at rather high Rm.

Figures 15 and 16 show the values of λ, ω, and A as functions of Rm for different boundary conditions, obtained when fitting again $E_m(t)$ with $f(t) \propto [1 + A\cos(\omega t)]e^{\lambda t}$. Since the amplitudes A are not so reliable when modifying the boundary conditions (because of the addition of the magnetic energy contained within the sidewalls), we will primarily rely on ω. The complete picture of derived dynamo thresholds can be found in Fig. 17. The blue curve in Fig. 15 and the green curve in Fig. 16 represent the reference cases without a sidewall. We recall that the eigenmodes were previously labeled as dipolar or quadrupolar in relation with the oscillatory features from Table I.

TABLE III. Dynamo thresholds in different configurations with or without an added conducting sidewall. The reference cases are made of the fluid-filled cylinder subject to VTC or in contact with a vacuum outer shell. The cases with a specified electrical conductivity refer to geometries with an added sidewall of thickness 0.03R and its magnetic permeability relative to the fluid $\mu_r^S = 1$. In those cases, the container is immerged in an insulating medium. Bold thresholds show oscillatory features of the quadrupole when in a symmetric column and of the dipole when in an antisymmetric column (see Table I). Thresholds above $\mathrm{Rm}^c = 2000$ were computed by extrapolating from the dominant eigenmodes at Rm = 1900, 2000, which are nonoscillatory.

Boundary conditions	Ref VTC		Ref vacuum		$\sigma_r^S = 0.125$		$\sigma_r^S = 4.5$	
Average velocity field/ eigenmode symmetry	sym	anti	sym	anti	sym	anti	sym	anti
Po = 0.100, $\mathrm{E}_{\mathrm{kin}}^{\mathrm{high}}$	**805**	·	**1147**	·	**1098**	·	·	**650**
Po = 0.100, $\mathrm{E}_{\mathrm{kin}}^{\mathrm{high}}$ symmetrized	**806**	**1263**	**1147**	**1649**	**1090**	**1493**	4372	**650**
Po = 0.100, $\mathrm{E}_{\mathrm{kin}}^{\mathrm{low}}$	·	**713**	·	**1009**	·	**894**	·	**615**
Po = 0.100, $\mathrm{E}_{\mathrm{kin}}^{\mathrm{low}}$ symmetrized	**777**	**677**	**1227**	**946**	**1531**	**897**	3037	**615**

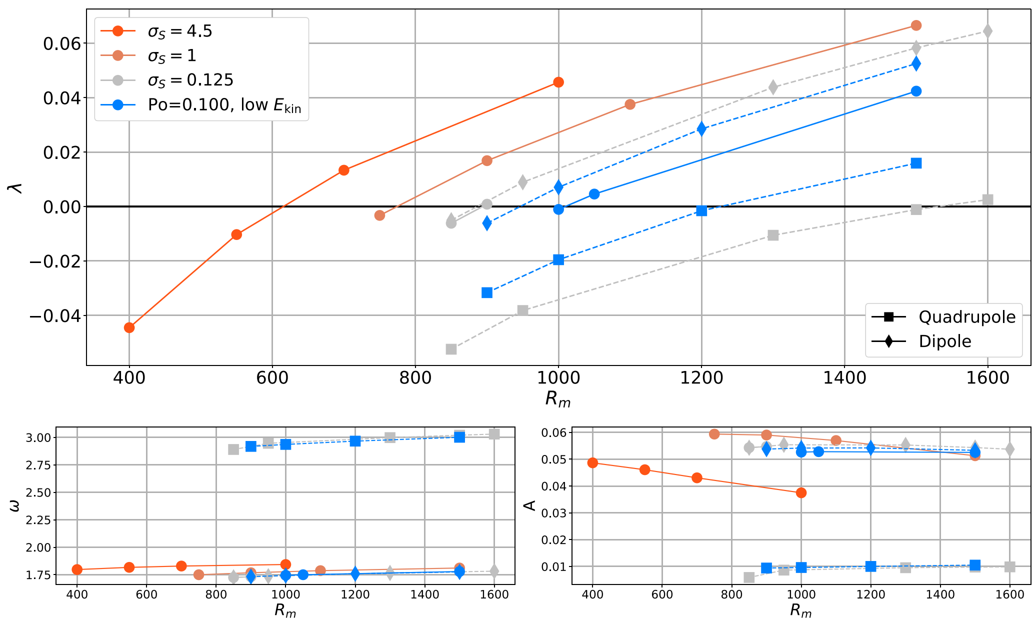

FIG. 15. Kinematic dynamo characteristics at Po = 0.100 using the low level velocity field. The plots represent the growth rate λ and the oscillation parameters, namely the angular frequency ω and the amplitude A, of the magnetic energy as functions of Rm. The fits are performed using the function $f(t) \propto [1 + A\cos(\omega t)]e^{\lambda t}$. Colors ranging from orange to gray map decreasing values of the electrical conductivity of the added sidewall with thickness $R = 0.03$. Its magnetic permeability is $\mu_r^S = 1$. No wall is added at the lids. The blue curves are the same as in Fig. 14 and constitute the reference configuration with vacuum and no conducting wall. For the latter, solid lines were computed using the full velocity field while dashed lines only considered the symmetric component of the velocity field in order to keep track of both $\mathbf{B}_{\mathrm{sym}}$ (quadrupole, square markers) and $\mathbf{B}_{\mathrm{anti}}$ (dipole, diamond markers) at the same time.

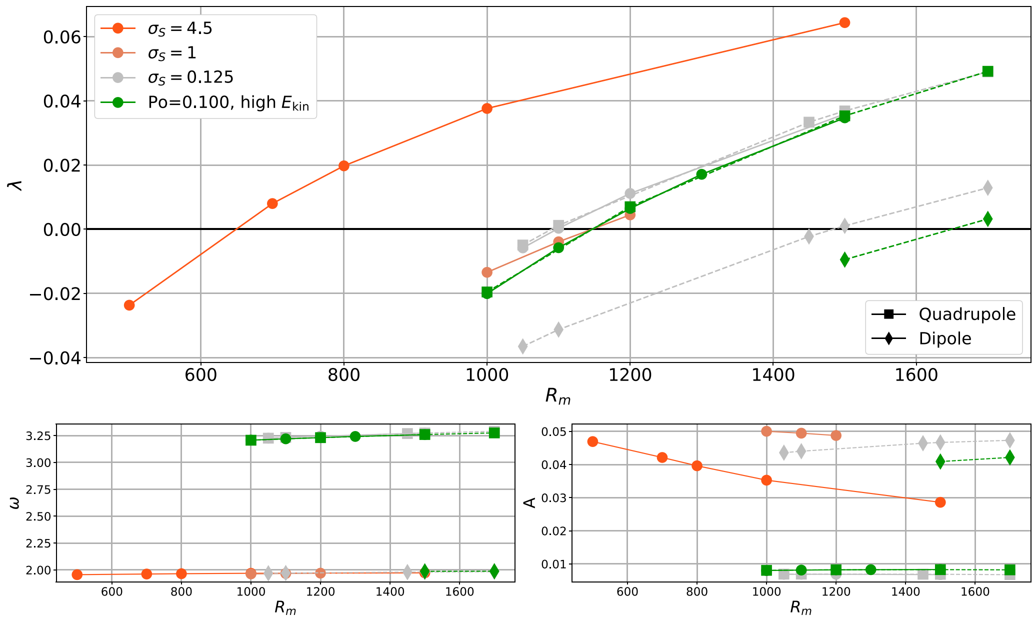

FIG. 16. Kinematic dynamo characteristics at $\mathrm{Po} = 0.100$ using the high level velocity field. The plots represent the growth rate λ and the oscillating parameters, namely the angular frequency ω and the amplitude A, of the magnetic energy as functions of Rm. The fits are performed using the function $f(t) \propto [1 + A\cos(\omega t)]e^{\lambda t}$. Colors ranging from orange to gray map decreasing values of the electrical conductivity of the added sidewall with thickness $R = 0.03$. Its magnetic permeability is $\mu_r = 1$. No wall is added at the lids. The green curves are not the same as in Fig. 14. They show a behavior in between the cases $\mathrm{Po} = 0.100$, $E_{\mathrm{kin}}^{\mathrm{high}}$ and $\mathrm{Po} = 0.099$, $E_{\mathrm{kin}}^{\mathrm{low}}$. It is the reference configuration with vacuum and no conducting wall . Solid lines were computed using the full velocity field, while dashed lines only considered the symmetric component of the velocity field in order to keep track of both $\mathbf{B}_{\mathrm{sym}}$ (quadrupole, square markers) and $\mathbf{B}_{\mathrm{anti}}$ (dipole, diamond markers) at the same time.

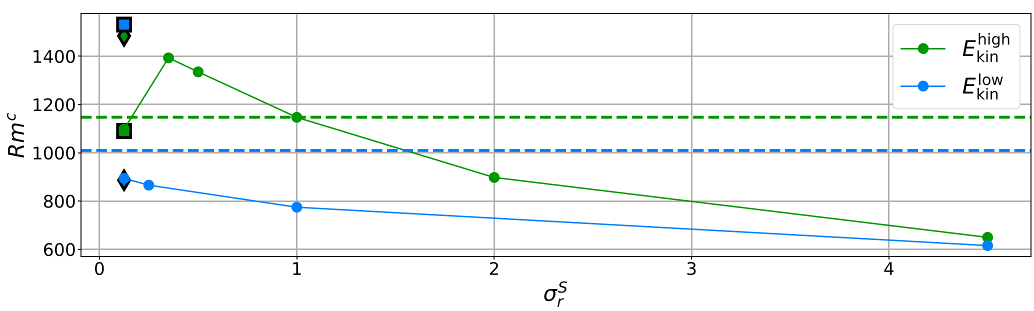

FIG. 17. Dynamo threshold Rm^c as a function of σ_r^S, the electrical conductivity of the sidewall. Its magnetic permeability is fixed at $\mu_r^S = 1$. Two velocity fields are considered: $\mathrm{Po} = 0.100$, $E_{\mathrm{kin}}^{\mathrm{high}}$ and $E_{\mathrm{kin}}^{\mathrm{low}}$. No wall is added at the lids. Straight lines connect dynamo thresholds computed with different sidewall electrical conductivities for the two fixed nonsymmetrized velocity fields. Dots surrounded by black were computed using the symmetrized velocity fields in order to keep track of both $\mathbf{B}_{\mathrm{sym}}$ (quadrupole, square markers) and $\mathbf{B}_{\mathrm{anti}}$ (dipole, diamond markers) simultaneously. They are only computed at $\sigma_r^S = 0.125$. Note that two of these points coincide almost perfectly with the nonsymmetrized equivalent. Dashed lines are the corresponding reference no-wall configurations.

First focusing on the $E_{\mathrm{kin}}^{\mathrm{low}}$ case (Fig. 15), we see that the dynamo threshold is reduced by the added sidewall, regardless of the value of σ_r (see the blue curve in Fig. 17). This improvement is of around 5.2% at $\sigma_r^S = 0.125$ while the benefit is of 35% when using $\sigma_r^S = 4.5$, displaying an even lower dynamo threshold than in the VTC reference case. This result aligns with that of [45,64], where a copper sidewall was found to be highly beneficial for dynamo action (a similar impact was observed in simulations of the VKS experiment [65]). Not surprisingly, as σ_r^S decreases, the value of Rm^c for the generated dipole approaches that of the reference configuration (dashed blue line in Fig. 17), which is consistent with the vacuum being modeled by a poorly conductive layer.

All this changes significantly when we consider the $E_{\mathrm{kin}}^{\mathrm{high}}$ case (Fig. 16). While the dominant magnetic mode in the reference configuration was the quadrupole, most runs involving an added sidewall now reveal a growing dipole. As before, Rm^c is reduced by 43% when the sidewall is made of copper, reaching a point where it even falls below the VTC reference case. This time, however, low electrical conductivity can lead to dynamo thresholds that are even *higher* than in the no-wall reference case (dashed green line in Fig. 17). Indeed, for $\sigma_r^S = 0.35$ (Fig. 17), Rm^c shows an increase of around 20%. When decreasing σ_r^S further to 0.125, we find that the dynamo threshold falls back to $\mathrm{Rm}^c = 1097$ and that the growing mode now shows oscillatory features of the quadrupole, as opposed to all other sidewall simulations with either $E_{\mathrm{kin}}^{\mathrm{high}}$ or $E_{\mathrm{kin}}^{\mathrm{low}}$. Such nonmonotonic behavior of $\mathrm{Rm}^c(\sigma_r^S)$ was also observed in simulations of the Riga experiment [66] where an oscillatory dynamo was obtained.

The mode crossing between dipolar and quadrupolar modes that explains nonmonotonicity when decreasing σ_r^S supports the idea that the growing eigenmode from the reference insulating case should be recovered as the electrical conductivity of the sidewall tends to 0. This is confirmed by runs performed using a symmetrized velocity field for the two cases (see Table III). Such simulations were performed at $\sigma_r^S = 4.5$ as well as $\sigma_r^S = 0.125$ for both high and low levels of kinetic energy. At $\sigma_r^S = 4.5$, all symmetric eigenmodes are exponentially decreasing up to $\mathrm{Rm} = 2000$, and those decreasing modes are nonoscillatory while the oscillating features of the antisymmetric eigenmode are those of the dipolar mode both for $E_{\mathrm{kin}}^{\mathrm{low}}$ (dipole in the reference case) and for $E_{\mathrm{kin}}^{\mathrm{high}}$ (quadrupole in the reference case). As for the simulations using $\sigma_r^S = 0.125$, both velocity fields are able to produce the oscillating dipole and quadrupole modes from Table III for $\mathrm{Rm} < 2000$. In both cases, the dominant mode matches the one expected from the reference case.

In a nutshell, the thresholds of the dipole and quadrupole appear to respond differently to the addition of a conductive sidewall with $0.25 \leqslant \sigma_r \leqslant 4.5$: the dipole's threshold is always decreased by the added sidewall (with a great impact for not too low electrical conductivities), while the quadrupole's threshold is greatly increased, with an exception made for $\sigma_r = 0.125$, where the threshold is close to that of the reference case. This difference can be understood when looking at Figs. 10(a) and 10(b): while the quadrupole exhibits six cells, the dipole shows only four. The effect of an added conductive sidewall is then to promote the emergence of large-scale structures, as they are typical for the dipole. Visualizations of the dipole with the added copper-made sidewall (not shown) indeed exhibit cells that occupy larger volumes than in the reference cases, especially near the cylinder's corners. Hence, it can favor the merging of two pairs of cells into one, i.e., the switch from a quadrupole (three pairs of cells) to a dipole (two pairs of cells).

It is also worthwhile comparing our results with those of Sec. A.2 of [45]. That section considered the same hydrodynamic setup discussed in our Sec. III B, with hydrodynamic parameters ($\mathrm{Re} = 1200$ and $\mathrm{Po} = 0.15$) which resemble ours to some extent. The magnetic field obtained in the no-wall situation of [44] could be labeled as quadrupolar. As shown in [45], this quadrupole transformed into an equatorial dipole when adding the sidewall. From the oscillations of the growing modes from Fig. 14(a) of [45], we can derive a frequency of 1.97 ± 0.05, which is indeed consistent with the values from Figs. 15 or 16 at $\sigma_r^S = 4.5$. While the antisymmetric eigenmode (dipole's) dynamo threshold is found to be decreased when increasing the sidewall's electrical conductivity, and conversely for the symmetric eigenmode (quadrupole), Ref. [50] finds a somewhat opposite conclusion. The growing oscillatory eigenmode is antisymmetric (dipolelike) and its dynamo threshold

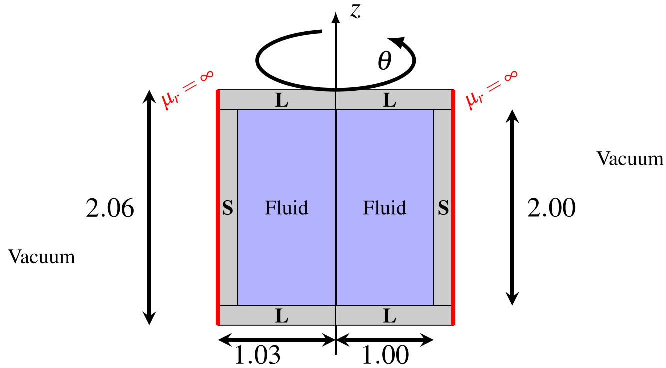

FIG. 18. Sketch of the hybrid VTC-vacuum configuration. L and S stand for Lid and Side. The interfaces highlighted in red have magnetic permeability $\mu_r^c = \infty$. The fluid-filled cylinder has dimensions $\{0 \leqslant r \leqslant 1, -1 \leqslant z \leqslant 1\}$. The lid and sidewalls have a thickness of 0.03. The sketch is not at scale.

is found to be significantly increased when increasing the sidewall's electrical conductivity, meaning it behaves as our quadrupole, and not as our dipole as we might have expected. This comes on top of the differences in oscillation frequencies discussed at the end of Sec. III B: differences can be expected regarding the impact of boundary conditions if we were to continuously follow the two eigenmodes described from our hydrodynamical parameter Re = 6500, Po $\sim$ 0.1 to those of [50], i.e., Re = 10 000, Po $\sim$ 0.1.

D. Impact of magnetic boundary conditions

For various technical reasons, the flow in the DRESDYN experiment is limited to Rm $\sim$ 700. While a significant decrease in the Rm^c-values obtained so far can be expected when increasing Re [see Fig. 8(b) of [39]], it is worthwhile looking for additional ways of lowering the dynamo threshold. Technically, it is still feasible to fix a thin sheet of mu-metal with $\mu_r \sim 10^5$ to the outer part of the sidewall, with the aim of emulating VTC boundary conditions according to the asymptotic behavior:

$$\frac{\mathbf{B}_1}{\mu_0} \times \mathbf{n}_1 = \frac{\mathbf{B}_2}{\mu_0 \mu_r} \times \mathbf{n}_2 \underset{\mu_r \to \infty}{\Rightarrow} \mathbf{B}_1 \times \mathbf{n}_1 = \mathbf{0}.$$

As observed in Sec. III B, VTC boundary conditions indeed decrease Rm^c by nearly 30% compared with the values for vacuum boundary conditions.

In this section, we therefore enhance the model developed in Sec. III C by first adding to the sidewall of thickness $0.03R$ a lid wall of the same thickness. To reflect the experimental conditions, the walls have magnetic permeability and electrical conductivity of, respectively, $(\mu_r^S, \sigma_r^S) = (1, 0.125)$ and $(\mu_r^L, \sigma_r^L) = (1, 0.125)$. In the following, we only consider one generating velocity field, namely the case Po = 0.100 (high E_{kin}) as studied in Sec. III C (distinct from the one labeled as such in Sec. III B), which gave rise to a growing quadrupole eigenmode. Moreover, we restrict this study to simulations with the raw velocity field.

While, from a numerical point of view, it would be easier to model the system with VTC boundary conditions imposed all over the container, such a model would not correspond to the experimental situation. To simulate VTC boundary conditions on the sidewall and vacuum boundary conditions on the lid walls, we propose a new setup (sketched in Fig. 18): instead of imposing continuity conditions across the interface between conductor and insulator at $r = 1.03$, we want to impose the condition $\mu_r(r = 1.03, |z| \leqslant 1.03) = \infty$. The jump conditions across this interface thus become VTC boundary conditions for $\mathbf{H}^{\mathrm{conductor}}$ on the one hand, and Dirichlet boundary conditions for the magnetic scalar potential $\phi = \mathrm{cst}$ on the other hand (which is equivalent to VTC boundary conditions $\nabla\phi^{\text{insulator}} \times \mathbf{n} = \mathbf{0}$). Meanwhile, the usual continuity conditions are maintained across the interfaces at $\{0 \leqslant r \leqslant 1.03,\ z = \pm 1.03\}$. This system will be called hybrid VTC-vacuum, or "VTC-vac" for short.

The VTC and vacuum configurations exhibit dynamo thresholds very similar to those of the simulations performed without the poorly conducting lid layer and sidewalls (see references in Table III). A similar correspondence was also observed in [37]. As expected, the hybrid VTC-vacuum configuration shows a dynamo threshold that lies between $\mathrm{Rm}^c_{\mathrm{VTC}}$ and $\mathrm{Rm}^c_{\mathrm{vacuum}}$. It is, however, much closer to $\mathrm{Rm}^c_{\mathrm{VTC}}$ than to $\mathrm{Rm}^c_{\mathrm{vacuum}}$: $\mathrm{Rm}^c_{\mathrm{VTC}}$ is 3.5% lower than $\mathrm{Rm}^c_{\text{VTC-vac}}$ while $\mathrm{Rm}^c_{\mathrm{vacuum}}$ is 34% higher than $\mathrm{Rm}^c_{\text{VTC-vac}}$. In other words, the tremendous gain from $\mathrm{Rm}^c_{\mathrm{vacuum}}$ to $\mathrm{Rm}^c_{\mathrm{VTC}}$ is almost recovered when only partially imposing VTC boundary conditions. This means that fixing a mu-metal thin sheet to the sidewall of the experimental vessel brings the dynamo threshold close to that computed with VTC boundary conditions, despite the magnetic field lines being free at the lids. Figures 8 and 12 indeed showed that the magnetic energy isosurfaces mostly map the cylinder's sidewall. Moreover, clear structures of quadrupoles or dipoles are observed for magnetic field lines emerging from the sidewall, while the maximum values of $\mathbf{H} = \nabla\phi$ in the insulating domain were observed close to the sidewall, at the interface between conducting and insulating domains (not shown).

Generally speaking, imposing VTC boundary conditions at an interface forces the Poynting flux to be zero at that location, thereby preventing magnetic energy from leaking. A way of understanding the proximity between $\mathrm{Rm}^c_{\mathrm{VTC}}$ and $\mathrm{Rm}^c_{\text{VTC-vac}}$ would therefore be to quantify the Poynting fluxes associated with the lid walls on the one hand and with the sidewall on the other hand. In Appendix, we provide numerical evidence that increasing μ_r at an interface should asymptotically tend to imposing VTC boundary conditions. Increasing the value of the relative magnetic permeability at a single given interface was also observed to significantly decrease the dynamo threshold in other experiments: in the Karlsruhe experiment [67] at the sidewall, and in the VKS experiment at the impellers [68].

IV. DISCUSSION AND OUTLOOK

The aim of this paper was to corroborate the findings of [36] that a precession-driven flow in a cylinder with an aspect ratio of 2 exhibits a strikingly low critical magnetic Reynolds number Rm^c within a certain range of the Poincaré number. In this narrow window, which is close to the transition between a weakly turbulent (or even laminar) to a highly turbulent state, the flow acquires an axisymmetric double-vortex roll. In the parlance of [49], this roll represents an $s2$ poloidal flow structure, which, jointly with the $t1$ zonal flow, is indeed prone to dynamo action at low Rm^c. Clearly, in the real precession-driven flow, things are more complicated due to the concurrent presence of the nonaxisymmetric $m = 1$ mode.

The remarkably low value of $\mathrm{Rm}^c \approx 430$ as derived by [36] was encouraging for the DRESDYN precession experiment, which is designed to reach $\mathrm{Rm} = 700$ [7]. However, this value was derived when the vanishing tangential component (VTC) boundary condition was applied to the magnetic field. Therefore, one of the main objectives of this paper was to analyze how the dynamo threshold depends on various boundary conditions, taking into account the technical constraints and remaining options of the DRESDYN experiment.

The second goal was to analyze in detail the spatial structure of the magnetic field eigenmodes expected to be produced by the dynamo. Building on previous studies [38,39], we demonstrated the presence of two distinct eigenmodes in close proximity. The dominance of these modes depends sensitively on the specifics of the flow. The first of these eigenmodes, which is symmetric in terms of centrosymmetry, is a quadrupole dominated by the azimuthal modes $m = 2$ and 3. The other one, which is antisymmetric, is a dipole dominated by the $m = 1$ and 2 modes.

In either case, the concurrent presence of two azimuthal components separated by $\Delta m = 1$ is quite natural due to the induction effect of the $m = 1$ flow component. Both multiple-component eigenmodes of the precession dynamo show a vacillation of the energy evolution. This is in

TABLE IV. Dynamo thresholds depending on the boundary conditions. All configurations have side and lid walls with thickness $0.03R$ and parameters $(\mu_r^{S/L}, \sigma_r^{S/L}) = (1, 0.125)$. The "hybrid VTC-vacuum" configuration considers VTC boundary conditions along the sidewall and continuity conditions across the lid walls (see Fig. 18). The quadrupolar mode is the dominant one in all three cases.

Configurations	VTC	hybrid VTC-vacuum	vacuum
Rm^c	805	834	1117

contrast, for example, with the pure $m = 1$ eigenfield of the Riga dynamo that is generated by its axisymmetric flow field.

As for the role of the boundaries, we generally observed an increase of around 30% when replacing the simplified VTC conditions with the vacuum boundary conditions (see Table II). These results are consistent with those obtained for kinematic dynamos, as in [57], or for the von Kármán sodium dynamo at $\mathrm{Re} = 1500$, where, depending on the magnetic permeability of the impellers, the reduction in the dynamo threshold ranged from $\mathrm{Rm}^c \approx 310$ (with vacuum BC) to $\mathrm{Rm}^c \approx 190$ (with VTC BC) or from $\mathrm{Rm}^c \approx 130$ (with vacuum BC) to $\mathrm{Rm}^c \approx 90$ (with VTC BC); see Table 3 in [55]. Significant reductions in Rm^c (in some cases even below the values for VTC) were observed here when using high-conductivity sidewalls, such as copper (see Table III). While this is barely a viable option given the other technical demands on the vessel, we also studied the effect of a sheet of high-mu material at the outer rim of the 3 cm stainless steel wall (see Table IV). Not surprisingly, this technically feasible measure would reduce the Rm^c values to a level almost identical to those for VTC conditions. As a result, starting from the very first liquid sodium experimental campaign, the vessel will be enhanced with this side high-mu material.

In any case, even the most optimistic values of Rm^c obtained here were in the range 600–800, as opposed to the value of 430 derived in [36]. While some of this discrepancy may be due to the more direct coupling between the flow and magnetic fields, we attribute much of it to the relatively low Reynolds number of 6500 used in the present paper. As shown in [39], the critical Rm^c drops significantly when Re is increased to 10 000. However, no clear trend can be inferred from these results, particularly because the velocity fields associated with the respective Reynolds numbers differ, leaving their comparability uncertain (e.g., the deviation from the respective optimal velocity field). For this purpose, kinematic dynamo simulations with analytically prescribed flow structures and varying amplitudes would be more appropriate, as they would allow us to model the effect of faster rotation (i.e., higher Re) in a systematic manner.

On the one hand, this strongly suggests extending the computations carried out here to higher values of Re. On the other hand, it is also clear that only the experiment (planned at $\mathrm{Re} \approx 10^8$) can ultimately validate the viability of our estimations.

A more straightforward direction for extending our work is to other nutation angles. As shown by [39], a variation between 60° prograde and 60° retrograde precession leads to significant changes in the flow structures in general, and in the transition point between weakly and strongly turbulent flows in particular. Quite generally, for prograde precession, this transition occurs at lower Poincaré numbers than for retrograde precession. While simulations suggest an optimum nutation angle of between 90° and 75° for retrograde precession, it is the position of the double-roll mode with respect to the transition point that is arguably the most important factor. The most critical issue here is that the motor's available torque (∼20 kNm) and power (∼1 MW) may not be sufficient to drive the flow in the fully turbulent regime at a vessel rotation rate above ∼5 Hz.

In the future, related investigations may also be carried out for blades mounted at the lids of the container, which provide an additional degree of freedom to impact the structure and the amplitude of the flow. Direct numerical simulations showed that the related increase of forcing shifts the transition point between the two flow regimes [69] and indeed allows a stronger flow amplitude in the laminar regime.

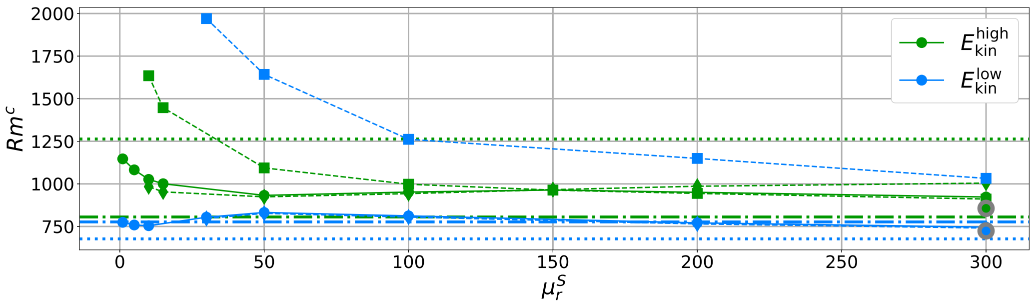

FIG. 19. Dynamo threshold Rm^c as a function of the relative magnetic permeability μ_r^S of the sidewall. Its electric conductivity is fixed at $\sigma_r^S = 1$ except for the dots surrounded by gray, for which we used the conductivity of stainless steel, $\sigma_r^S = 0.125$. No wall is added to the lids. Two velocity fields are considered: $\mathrm{Po} = 0.100$, with either a high or a low level of kinetic energy (see Table III). Straight lines correspond to the full velocity field while for the dashed lines we only consider the symmetric component of the velocity field in order to keep track of both $\mathbf{B}_{\mathrm{sym}}$ (quadrupole, square markers) and $\mathbf{B}_{\mathrm{anti}}$ (dipole, diamond markers) at the same time. The horizontal lines are the reference VTC dynamo thresholds (see columns 3 and 4 of Table III), dotted being the quadrupole and dash-dot the dipole.

ACKNOWLEDGMENTS

V.B. and C.N. would like to thank Jean-Luc Guermond (TAMU, USA) for helpful discussions and acknowledge the support of the Agence Nationale de la Recherche through the MilaDy project (ANR-25-CE51-0077-02). This work was granted access to the HPC resources of IDRIS under the allocation 2025-[A0182A00254] made by GENCI. It has also been supported by Deutsche Forschungsgemeinschaft (DFG) under Project No. 532905681.

DATA AVAILABILITY

The data that support the findings of this article are not publicly available upon publication because it is not technically feasible and/or the cost of preparing, depositing, and hosting the data would be prohibitive within the terms of this research project. The data are available from the authors upon reasonable request.

APPENDIX

In this Appendix, we provide numerical evidence that increasing μ_r at an interface should asymptotically tend to imposing of VTC boundary conditions. The system we consider is similar to that of Sec. III C: the fluid-filled cylinder is supplemented with a $0.03R$-thick conducting sidewall, whereas no lid walls are considered. The sidewall is assumed to have electrical conductivity $\sigma_r^S = 1$ and a magnetic permeability μ_r^S ranging from 1 to 300. We use the same velocity fields as in Sec. III C. They are taken either raw or symmetrized, and their associated dynamo thresholds (for $\mu_r^S = 1$) were given in Table III. The thresholds obtained for these four velocity fields as functions of μ_r^S are shown in Fig. 19. What we would like to show is that increasing μ_r^S is equivalent to applying mixed boundary conditions viz. VTC on the sidewall and vacuum on the lid walls. As a reference, therefore, we will use the values of the VTC simulations reported in Table III.

We first focus on the raw velocity field (solid lines). The data for $\mu_r^S = 1$ match the results detailed in Sec. III C at $\sigma_r^S = 1$. Then, as μ_r^S is increased, $\mathrm{Rm}^c(\mu_r^S)$ shows a nonmonotonous behavior, with local minima, $\mu_{r,\min}^{S,\mathrm{high}} \sim 50$ and $\mu_{r,\min}^{S,\mathrm{low}} \sim 15$, followed by local maxima, $\mu_{r,\max}^{S,\mathrm{high}} \sim 150$ and $\mu_{r,\max}^{S,\mathrm{low}} \sim 50$, and eventually by a decrease of $\mathrm{Rm}^c(\mu_r^S)$ for increasing $\mu_r^S \gtrsim 200$. A finer picture of $\mathrm{Rm}^c(\mu_r^S)$ emerges when considering the symmetrized velocity fields (dashed lines). The square and diamond markers indicate that the eigenmode exhibits quadrupolar and dipolar oscillatory features, respectively (see Table I). As expected from Sec. III C, at low μ_r^S the first unstable eigenmode is the dipolar mode for a nonmagnetic and conducting sidewall, while no quadrupole mode appears at such magnetic parameters. Bearing in mind that the VTC symmetrized reference configurations (see Table III) generate both unstable quadrupolar and dipolar modes for $\mathrm{Rm} < 2000$, we expect the quadrupole mode to become unstable for lower Rm as $\mu_r^{S,\mathrm{high}}$ or $\mu_r^{S,\mathrm{low}}$ are increased. Indeed, our simulations produce values of $\mathrm{Rm}^c_{\mathrm{quadrupole}}(\mu_r^S) < 2000$ when μ_r^S becomes high enough, namely $\mu_r^{S,\mathrm{high}} \gtrsim 10$ and $\mu_r^{S,\mathrm{low}} \gtrsim 30$. From these limit values of magnetic permeability onward, $\mathrm{Rm}^c_{\mathrm{quadrupole}}(\mu_r^S)$ monotonically decreases until the largest magnetic permeability $\mu_r^S = 300$.

As for the dipolar mode, its dynamo threshold $\mathrm{Rm}^c_{\mathrm{dipole}}$ is below 2000 for all simulated $\mu_r^{S,\mathrm{high/low}}$. In the case of $E_{\mathrm{kin}}^{\mathrm{low}}$, we observe an almost perfect match of the dynamo thresholds associated with the magnetic eigenmode from the raw velocity field on the one hand and the antisymmetric eigenmode from the symmetrized velocity field on the other hand. The case $E_{\mathrm{kin}}^{\mathrm{high}}$ differs, however. Indeed, $\mathrm{Rm}^c_{\mathrm{dipole}}(\mu_r^{S,\mathrm{high}})$ shows the same local minimum of dynamo threshold as the equivalent raw simulations, but not a local maximum. Instead, it is continuously increasing with $\mu_r^{S,\mathrm{high}}$ until $\mu_r^{S,\mathrm{high}} = 300$. Most importantly, we observe a mode crossing at $\mu_r^{S,\mathrm{high}} \sim 150$ between the quadrupolar and the dipolar modes, with the quadrupolar mode becoming the first unstable magnetic mode for $\mu_r^{S,\mathrm{high}} > 150$. This is compatible with the results from the VTC reference configuration using $E_{\mathrm{kin}}^{\mathrm{high}}$, for which the quadrupolar mode is indeed the first unstable magnetic mode.

To summarize, the dynamo thresholds from the raw simulations of $E_{\mathrm{kin}}^{\mathrm{low}}$ are perfectly explained by those of the dipolar mode computed from the symmetrized equivalent, while the velocity field $E_{\mathrm{kin}}^{\mathrm{high}}$ generates dynamo action with mode crossing between the dipolar and quadrupolar mode. In fact, the behavior at low $\mu_r^{S,\mathrm{high}}$ is explained by the dipolar mode and that at high $\mu_r^{S,\mathrm{high}}$ by the quadrupolar mode. The suggested monotonicities of $\mathrm{Rm}^c_{\mathrm{quadrupole/dipole}}(\mu_r^{S,\mathrm{high/low}})$ at $\mu_r^S > 150$ are compatible with the dynamo thresholds provided in Table III and sketched in Fig. 19, which can therefore be considered as limits of Rm^c for high μ_r^S. However, naive linear extrapolations of $\mathrm{Rm}^c(\mu_r^S)$ for high values of μ_r^S suggest that the limit could only be reached for $\mu_r^S > 1000$, which is computationally too expensive.

---

[1] M. Landeau, A. Fournier, H.-C. Nataf, D. Cebron, and N. Schaeffer, Sustaining Earth's magnetic dynamo, Nat. Rev. Earth Environ. **3**, 255 (2022).

[2] J. Vidal and D. Cebron, Did lunar tides sustain the early earth's dynamo? C. R. Geosci. **358**, 1 (2026).

[3] C. A. Dwyer, D. J. Stevenson, and F. Nimmo, A long-lived lunar dynamo driven by continuous mechanical stirring, Nature (London) **479**, 212 (2011).

[4] R. R. Fu, B. P. Weiss, D. L. Shuster, J. Gattacceca, T. L. Grove, C. Suavet, E. A. Lima, L. Li, and A. T. Kuan, An ancient core dynamo in asteroid Vesta, Science **338**, 238 (2012).

[5] G. Consolini and P. De Michelis, Stochastic resonance in geomagnetic polarity reversals, Phys. Rev. Lett. **90**, 058501 (2003).

[6] A. Gailitis, O. Lielausis, E. Platacis, G. Gerbeth, and F. Stefani, Colloquium: Laboratory experiments on hydromagnetic dynamos, Rev. Mod. Phys. **74**, 973 (2002).

[7] F. Stefani, Liquid-metal experiments on geophysical and astrophysical phenomena, Nat. Rev. Phys. **6**, 409 (2024).

[8] A. Gailitis, O. Lielausis, S. Dement'ev, E. Platacis, A. Cifersons, G. Gerbeth, T. Gundrum, F. Stefani, M. Christen, H. Hänel, and G. Will, Detection of a flow induced magnetic field eigenmode in the Riga dynamo facility, Phys. Rev. Lett. **84**, 4365 (2000).

[9] A. Gailitis, O. Lielausis, E. Platacis, S. Dement'ev, A. Cifersons, G. Gerbeth, T. Gundrum, F. Stefani, M. Christen, and G. Will, Magnetic field saturation in the Riga dynamo experiment, Phys. Rev. Lett. **86**, 3024 (2001).

[10] A. Gailitis, G. Gerbeth, T. Gundrum, O. Lielausis, G. Lipsbergs, E. Platacis, and F. Stefani, Self-excitation in a helical liquid metal flow: The Riga dynamo experiments, J. Plasma Phys. **84**, 735840301 (2018).
[11] R. Stieglitz and U. Müller, Experimental demonstration of a homogeneous two-scale dynamo, Phys. Fluids **13**, 561 (2001).
[12] U. Müller, R. Stieglitz, and S. Horanyi, A two-scale hydromagnetic dynamo experiment, J. Fluid Mech. **498**, 31 (2004).
[13] U. Müller, R. Stieglitz, F. H. Busse, and A. Tilgner, The Karlsruhe two-scale dynamo experiment, C. R. Phys. **9**, 729 (2008).
[14] M. Berhanu, R. Monchaux, S. Fauve, N. Mordant, F. Petrelis, A. Chiffaudel, F. Daviaud, B. Dubrulle, L. Marie, F. Ravelet, M. Bourgoin, P. Odier, J.-F. Pinton, and R. Volk, Magnetic field reversals in an experimental turbulent dynamo, Europhys. Lett. **77**, 59001 (2007).
[15] F. Ravelet, M. Berhanu, R. Monchaux, S. Aumaitre, A. Chiffaudel, F. Daviaud, B. Dubrulle, M. Bourgoin, P. Odier, N. Plihon, J. F. Pinton, R. Volk, S. Fauve, N. Mordant, and F. Petrelis, Chaotic dynamos generated by a turbulent flow of liquid sodium, Phys. Rev. Lett. **101**, 074502 (2008).
[16] R. Monchaux, M. Berhanu, S. Aumaitre, A. Chiffaudel, F. Daviaud, B. Dubrulle, F. Ravelet, S. Fauve, N. Mordant, F. Petrelis, M. Bourgoin, P. Odier, J.-F. Pinton, N. Plihon, and R. Volk, The von Karman sodium experiment: Turbulent dynamical dynamos, Phys. Fluids **21**, 035108 (2009).
[17] F. Stefani, G. Gerbeth, U. Günther, and A. Xu, Why dynamos are prone to reversals, Earth Planet. Sci. Lett. **243**, 828 (2006).
[18] F. Petrelis, S. Fauve, E. Dormy, and J.-P. Valet, Simple mechanism for reversals of Earth's magnetic field, Phys. Rev. Lett. **102**, 144503 (2009).
[19] R. Benzi and J.-F. Pinton, Magnetic reversals in a simple model of magnetohydrodynamics, Phys. Rev. Lett. **105**, 024501 (2010).
[20] F. Stefani, S. Eckert, G. Gerbeth, A. Giesecke, T. Gundrum, C. Steglich, T. Weier, and B. Wustmann, DRESDYN - A new facility for MHD experiments with liquid sodium, Magnetohydrodynamics **48**, 103 (2012).
[21] F. Stefani, A. Gailitis, G. Gerbeth, A. Giesecke, T. Gundrum, G. Rüdiger, M. Seilmayer, and T. Vogt, The DRESDYN project: Liquid metal experiments on dynamo action and magnetorotational instability, Geophys. Astrophys. Fluid Dyn. **113**, 51 (2019).
[22] F. Stefani, S. Anders, S. Eckert, N. Freyer, G. Gerbeth, A. Giesecke, T. Gundrum, P. Kaever, V. Kumar, F. Pizzi, D. Raebiger, J. Simkanin, C. Steglich, T. Vogt, N. Wagner, and G. Wedel, The DRESDYN precession experiment, C. R. Phys. **25**, 629 (2024).
[23] T. Sloudsky, De la rotation de la Terre suppose'e fluide a' son interieur, Bull. Soc. Imp. Nat. Moscou **9**, 285 (1895).
[24] H. Poincaré, Sur la précession des corps déformables, Bull. Astron. **27**, 321 (1910).
[25] F. H. Busse, Steady fluid flow in a precessing spheroidal shell, J. Fluid Mech. **33**, 739 (1968).
[26] R. Manasseh, Breakdown regimes of inertia waves in a precessing cylinder, J. Fluid Mech. **243**, 261 (1992).
[27] J. J. Kobine, Azimuthal flow associated with inertial wave resonance in a precessing cylinder, J. Fluid Mech. **319**, 387 (1996).
[28] Y. Lin, J. Noir, and A. Jackson, Experimental study of fluid flows in a precessing cylindrical annulus, Phys. Fluids **26**, 046604 (2014).
[29] W. Mouhali, T. Lehner, J. Léorat, and R. Vitry, Evidence of a cyclonic regime in a precessing cylindrical container, Exp. Fluids **53**, 1693 (2012).
[30] S. Goto, A. Matsunaga, M. Fujiwara, M. Nishioka, S. Kida, M. Yamato, and S. Tsuda, Turbulence driven by precession in spherical and slightly elongated spheroidal cavities, Phys. Fluids **26**, 055107 (2014).
[31] J. Herault, T. Gundrum, A. Giesecke, and F. Stefani, Subcritical transition to turbulence of a precessing flow in a cylindrical vessel, Phys. Fluids **27**, 124102 (2015).
[32] K. Komoda and S. Goto, Three-dimensional flow structures of turbulence in precessing spheroids, Phys. Rev. Fluids **4**, 014603 (2019).
[33] C. Nobili, P. Meunier, B. Favier, and M. Le Bars, Hysteresis and instabilities in a spheroid in precession near the resonance with the tilt-over mode, J. Fluid Mech. **909**, A17 (2021).

[34] J. Noir and D. Cébron, Precession-driven flows in non-axisymmetric ellipsoids, J. Fluid Mech. **737**, 412 (2013).

[35] F. Burmann and J. Noir, Experimental study of the flows in a non-axisymmetric ellipsoid under precession, J. Fluid Mech. **932**, A24 (2022).

[36] A. Giesecke, T. Vogt, T. Gundrum, and F. Stefani, Nonlinear large scale flow in a precessing cylinder and its ability to drive dynamo action, Phys. Rev. Lett. **120**, 024502 (2018).

[37] A. Giesecke, T. Vogt, T. Gundrum, and F. Stefani, Kinematic dynamo action of a precession-driven flow based on the results of water experiments and hydrodynamic simulations., Geophys. Astrophys. Fluid Dyn. **113**, 235 (2019).

[38] F. Pizzi, A. Giesecke, J. Šimkanin, and F. Stefani, Prograde and retrograde precession of a fluid-filled cylinder, New J. Phys. **23**, 123016 (2021).

[39] V. Kumar, F. Pizzi, A. Giesecke, J. Šimkanin, T. Gundrum, M. Ratajczak, and F. Stefani, The effect of nutation angle on the flow inside a precessing cylinder and its dynamo action, Phys. Fluids **35**, 014114 (2023).

[40] A. Giesecke, T. Vogt, F. Pizzi, V. Kumar, F. Garcia Gonzalez, T. Gundrum, and F. Stefani, The global flow state in a precessing cylinder, J. Fluid Mech. **998**, A30 (2024).

[41] A. Tilgner, Precession driven dynamos, Phys. Fluids **17**, 034104 (2005).

[42] C.-C. Wu and P. H. Roberts, On a dynamo driven by topographic precession, Geophys. Astrophys. Fluid Dyn. **103**, 467 (2009).

[43] A. Krauze, Numerical modeling of the magnetic field generation in a precessing cube with a conducting melt, Magnetohydrodynamics **46**, 271 (2010).

[44] C. Nore, J. Léorat, J.-L. Guermond, and F. Luddens, Nonlinear dynamo action in a precessing cylindrical container, Phys. Rev. E **84**, 016317 (2011).

[45] L. Cappanera, J.-L. Guermond, J. Léorat, and C. Nore, Two spinning ways for precession dynamo, Phys. Rev. E **93**, 043113 (2016).

[46] Y. Lin, P. Marti, J. Noir, and A. Jackson, Precession-driven dynamos in a full sphere and the role of large scale cyclonic vortices, Phys. Fluids **28**, 066601 (2016).

[47] O. Goepfert and A. Tilgner, Dynamos in precessing cubes, New J. Phys. **18**, 103019 (2016).

[48] J. Vidal and D. Cébron, Kinematic dynamos in triaxial ellipsoids, Proc. R. Soc. A **477**, 20210252 (2021).

[49] M. L. Dudley and R. W. James, Time-dependent kinematic dynamos with stationary flows, Proc. R. Soc. London A **425**, 407 (1989).

[50] A. Giesecke, M. Wilbert, J. Šimkanin, R. Grauer, and F. Stefani, The role of magnetic boundaries in kinematic and self-consistent magnetohydrodynamic simulations of precession-driven dynamo action in a closed cylinder, Phys. Fluids **37**, 086607 (2025).

[51] D. Kong, Z. Cui, X. Liao, and K. Zhang, On the transition from the laminar to disordered flow in a precessing spherical-like cylinder, Geophys. Astrophys. Fluid Dyn. **109**, 1 (2015).

[52] A. Giesecke, T. Albrecht, T. Gundrum, J. Herault, and F. Stefani, Triadic resonances in nonlinear simulations of a fluid flow in a precessing cylinder, New J. Phys. **17**, 113044 (2015).

[53] J.-L. Guermond, R. Pasquetti, and B. Popov, Entropy viscosity method for nonlinear conservation laws, J. Comput. Phys. **230**, 4248 (2011).

[54] J.-L. Guermond, R. Pasquetti, and B. Popov, From suitable weak solutions to entropy viscosity, J. Sci. Comp. **49**, 35 (2011).

[55] C. Nore, D. Castanon Quiroz, L. Cappanera, and J.-L. Guermond, Numerical simulation of the von kármán sodium dynamo experiment, J. Fluid Mech. **854**, 164 (2018).

[56] A. Bonito and J.-L. Guermond, Approximation of the eigenvalue problem for the time harmonic Maxwell system by continuous Lagrange finite elements, Math. Comp. **80**, 1887 (2011).

[57] A. Giesecke, C. Nore, F. Stefani, G. Gerbeth, J. Léorat, F. Luddens, and J.-L. Guermond, Electromagnetic induction in non-uniform domains, Geophys. Astrophys. Fluid Dyn. **104**, 505 (2010).

[58] A. Bonito, J.-L. Guermond, and F. Luddens, Regularity of the Maxwell equations in heterogeneous media and Lipschitz domains, J. Math. Anal. Appl. **408**, 498 (2013).

[59] J. M. Lopez and F. Marques, Nonlinear and detuning effects of the nutation angle in precessionally forced rotating cylinder flow, Phys. Rev. Fluids **1**, 023602 (2016).

[60] D. Gao, P. Meunier, S. Le Dizès, and C. Eloy, Zonal flow in a resonant precessing cylinder, J. Fluid Mech. **923**, A29 (2021).

[61] See Supplemental Material at http://link.aps.org/supplemental/10.1103/rx1h-5zxp for movies of the oscillating quadrupole and dipole, both in the cylinder vacuum regions.

[62] A. Giesecke, F. Stefani, and G. Gerbeth, Kinematic simulations of dynamo action with a hybrid boundary-element/finite-volume method, Magnetohydrodynamics **44**, 237 (2008).

[63] F. Pizzi, Numerical studies of a fluid-filled precessing cylinder: A framework for the DRESDYN precession experiment, Doctoral thesis, BTU Cottbus–Senftenberg (2023).

[64] F. Stefani, T. Albrecht, G. Gerbeth, A. Giesecke, T. Gundrum, J. Herault, C. Nore, and C. Steglich, Towards a precession driven dynamo experiment, Magnetohydrodynamics **51**, 275 (2015).

[65] F. Ravelet, A. Chiffaudel, F. Daviaud, and J. Léorat, Toward an experimental von Kármán dynamo: Numerical studies for an optimized design, Phys. Fluids **17**, 117104 (2005).

[66] R. Avalos-Zuniga, F. Plunian, and A. Gailitis, Influence of electromagnetic boundary conditions onto the onset of dynamo action in laboratory experiments, Phys. Rev. E **68**, 066307 (2003).

[67] R. Avalos-Zuñiga and F. Plunian, Influence of inner and outer walls electromagnetic properties on the onset of a stationary dynamo, Eur. Phys. J. B **47**, 127 (2005).

[68] A. Giesecke, C. Nore, F. Stefani, G. Gerbeth, J. Léorat, W. Herreman, F. Luddens, and J.-L. Guermond, Influence of high-permeability discs in an axisymmetric model of the Cadarache dynamo experiment, New J. Phys. **14**, 053005 (2012).

[69] M. Wilbert, A. Giesecke, and R. Grauer, Numerical investigation of the flow inside a precession-driven cylindrical cavity with additional baffles using an immersed boundary method, Phys. Fluids **34**, 096607 (2022).